Full length article

Characterizing microscale deformation mechanisms and macroscopic tensile properties of a high strength magnesium rare-earth alloy: A combined experimental and crystal plasticity approach

A. Githens [a], S. Ganesan [b], Z. Chen [c], J. Allison [a], V. Sundararaghavan [b], S. Daly [c],*

[a] *University of Michigan, Department of Materials Science and Engineering, USA*
[b] *University of Michigan, Department of Aerospace Engineering, USA*
[c] *University of California at Santa Barbara, Department of Mechanical Engineering, USA*

A B S T R A C T

The effect of aging on the accumulation of microscale plasticity, and the resulting macroscopic mechanical behavior, were examined in the magnesium alloy WE43 under uniaxial tension. Full-field strains on the length scale of the microstructure, and their relation to the underlying crystallography, were captured using a combination of electron backscatter diffraction, custom nanoparticle patterning processes for corrosion-susceptible alloys, scanning electron microscopy (SEM), in-SEM uniaxial tensile and compressive loading, and distortion-corrected digital image correlation. The as-received material exhibited an average grain size of 12 μm. The strain incurred on individual slip traces in magnesium was resolved for the first time. Insights into slip activation across the microstructure revealed that using Schmid's Law with the nominal Schmid Factor appeared to be predictive for basal and non-basal slip. The DIC results were compared with simulation using an advanced open-source crystal plasticity finite element (CPFE) code, PRISMS-Plasticity. The PRISMS-Plasticity model is a more precise determination of the local Schmid Factor and was used to simulate variations in slip and twin activity within each grain. Such simulations provide an avenue for physically interpreting the various slip traces observed in the dense DIC data and an improved understanding of the critical resolved shear stress of the various slip systems.

© 2019 Acta Materialia Inc. Published by Elsevier Ltd. All rights reserved.

1. Introduction

The deformation mechanisms of polycrystalline magnesium and its alloys are complex. To enable acceleration of the alloy development process, new approaches are required to characterize and quantify the details of operative slip and twinning mechanisms, and their dependence on alloying and heat treatment. In this paper, we outline an experimental and computational approach that relies on novel *in-situ* measurements of grain level surface strains combined with simulations from an open-source crystal plasticity finite element simulation tool, PRISMS-Plasticity [1–3]. The high strength magnesium alloy, WE43, in a hot-rolled and aged condition (T5), was used for this study.

Magnesium can plastically deform via slip on four independent systems and on two or more independent twinning systems. Slip occurs on the following planes and directions: basal slip $\{0001\} < 11\bar{2}0 >$, prismatic slip $\{10\bar{1}0\} < 11\bar{2}0 >$, pyramidal $<a>$ slip $\{10\bar{1}1\} < 11\bar{2}0 >$, and pyramidal $<c+a>$ slip $\{11\bar{2}2\} < 11\bar{2}3 >$.

The von Mises criterion dictates that there must be at least five independent deformation modes in a polycrystalline material to accommodate plastic deformation, so either the two twinning modes or pyramidal $<c+a>$ slip are required to support deformation. To accommodate c-axis extension, $\{10\bar{1}2\} < 10\bar{1}1 >$ twinning is often activated, also called tension or extension twinning due to the required *c*-axis tensile strain. To accommodate *c*-axis compression, $\{10\bar{1}1\} < 10\bar{1}2 >$ twinning is often activated, also called compression twinning due to the required *c*-axis compressive strain. Depending on the texture of the magnesium alloy, directionally dependent twinning events can lead to asymmetric tension-compression behavior [4–6].

Determining the value of the critical resolved shear stress (CRSS) for each deformation mode, and their relative contributions during plastic deformation, is the subject of considerable interest. In general, basal slip is significantly easier to activate compared to other systems. For the quasi-static loading of polycrystalline pure magnesium at room temperature, it is generally accepted that $CRSS_{basal} < CRSS_{tensile-twinning} < CRSS_{prismatic} < CRSS_{pyramidal}$ where grain size [7], temperature [8], alloying content [9], and precipitation strengthening [10] can affect these CRSS values. Experimental

efforts have estimated the CRSS ratios between systems for poly-crystalline HCP materials [11], but absolute values of the stresses cannot be measured directly. In contrast, computational models have been used to determine these values, but experimental data is still required to validate these predictions.

Elastoplastic self-consistent (EPSC) models, viscoplastic self-consistent (VPSC) models, [9,12,13] and finite element crystal plasticity models [14–18] are valuable tools for better understanding the CRSS and relative activation of the different slip systems during plastic deformation. Experimental validation for crystal plasticity based models has been primarily in the form of tension/compression flow curves, *in-situ* surface strain measurement [13], in-*situ* neutron diffraction [10], in-*situ* EBSD [8], and transmission electron microscopy (TEM) [12]. If models can accurately predict flow curves in magnesium alloys, a next logical step is to accurately predict full-field strains. However, experimental data on the full-field strain development during plastic loading is lacking, particularly when compared with computational modeling contributions. Full-field strains at the microstructural level reveal insights into strain heterogeneities on the surface, and their relationships to the local microstructure, that are averaged in the macroscopic stress-strain data.

A complicating factor in the experimental determination of CRSS for the various slip modes is the texture of the underlying material. In many wrought magnesium alloys, a basal texture is frequently observed, with the hcp *c*-axis orthogonal to the plate or extrusion processing axis. Twinning selection depends on the *c*-axis strain, and the propensity for twinning changes with loading direction. When a sample is loaded in tension parallel to the processing direction, the basal texture leads to contraction along the orthogonal *c*-axis. When the sample is loaded in compression parallel to the processing direction, the same texture effects lead to extension along the *c*-axis. This activates tensile twinning, a deformation mode with a low CRSS relative to the other non-basal systems. Tension and compression will thus activate different deformation mechanisms, which can cause a tension-compression asymmetry. Accurately predicting what deformation modes activate, and to what extent, is critical in the prediction of the global plastic behavior of magnesium alloys.

Optical deformation tracking methods, including digital image correlation, have been widely utilized to quantify the mechanical behavior of magnesium alloys at the macroscale and mesoscale. Digital Image Correlation (DIC) is a useful technique for characterizing macroscopic and microscopic surface strains. It tracks the deformation of a speckle pattern placed on a material surface during thermo-mechanical loading [19]. The technique is length scale independent, but a suitable speckle pattern must be applied to a surface at the desired field of view. Barnett et al. used DIC to characterize post-failure strain fields of a coarse-grained AZ31 specimen tested in tension [20]. They linked $\{10\bar{1}1\}$-$\{10\bar{1}2\}$ double twinning to high shear strain and void formation, causing early failure for this alloy. Stanford et al. used a grid-based method to map the surface deformations of AZ31, demonstrating that grain boundary sliding was not prevalent at either room or elevated temperature, but that the strain field became more homogenous as ambient temperature was increased [21]. Several papers [13,22,23] have addressed the use of crystal plasticity simulations to understand surface microstructure response characterized by methods such as Orientation Imaging Microscopy (OIM) and DIC. For example Ref [45] finds that the misorientations developed in the surface and bulk grains are different and accounting for grain equilibrium is essential for prediction of these misorientations.

Recent microscale experiments indicate that slip activity in Mg-rare-earth alloys can be pre-determined from the initial microstructure, where strain localization increases in magnitude but does not change spatially across the surface. Martin et al.

performed *in-situ* grid-based DIC studies of Mg-rare-earth alloys under tensile deformation [13,24]. In order to examine slip without significant twinning effects, Mg-rare-earth alloys undergoing tension parallel to the rolling direction were investigated. They demonstrated that strain accumulates at grain boundaries, and that localized strain appears at the onset of yielding and does not change location with increased plastic deformation. This experimental data was compared with crystal plasticity simulations, which suggest that high strains on grain boundaries occur in grain neighborhoods in which one grains is oriented to accommodate basal slip and an adjacent grain is oriented to prefer non-basal slip. Interestingly, Martin et al. found no statistically significant relationship between surface strain and grains with high nominal Schmid factors for basal slip [13]. Although it is convenient to use descriptors like nominal Schmid factor to predict strain, it appears this approach is overly simplistic, and that the neighborhood surrounding a grain strongly influences its deformation.

Rare-earth alloying additions have been observed to weaken the basal texture during rolling and extrusion processing [25,26] and thus improve the tensile ductility. A strong basal texture limits ductility by preventing the easy activation of slip. When a specimen with strong basal texture is loaded in uniaxial tension perpendicular to the processing direction (often referred to as the ND direction), the majority of grains are not oriented favorably to activate basal slip, as the basal plane normal is perpendicular to the loading direction. Non-basal systems with higher critical resolved shear stresses must be activated, which requires a higher stress state and reduces the total elongation to failure. With a weaker texture, more grains are favorably aligned to activate basal slip when loaded in uniaxial tension perpendicular to the ND, and the material elongates to a greater extent.

In the current work, interactions between microstructure and plasticity are examined across length scales in the WE43-T5 material. In the T5 condition, the WE43 plates exhibited a weak basal texture [27], shown in Fig. 1. Full-field strains on the length scale of the microstructure, and their relation to the underlying crystallography, were captured using a combination of electron backscatter diffraction (EBSD), custom nanoparticle patterning processes for corrosion-susceptible alloys [28], scanning electron microscopy (SEM), in-SEM uniaxial tensile and compression loading, and distortion-corrected digital image correlation (DIC). These experimental results are used to parameterize and validate a new open-source crystal plasticity finite element (CPFE) code, PRISMS-Plasticity, as described below and in [2,47].

2. Material and experimental methods

2.1. Uniaxial tension

The as-received material (WE43-T5) was a hot rolled and aged WE43 plate with an average grain size of 12 μm (number average) as calculated from EBSD data. An EBSD scan of step size 0.24 μm was taken across twelve different 80 μm by 80 μm fields of view to determine grain orientations. Fig. 2(a) shows an SEM image of a polished and etched tensile specimen, where the precipitates along grain boundaries are evident. As shown in the Fig. 2(a) inset, twins exist in the microstructure as a result of hot rolling. Precipitates have preferentially nucleated along these twin boundaries much in the same way they form along grain boundaries, suggesting that the twins form during the rolling process prior to aging.

Precipitation hardening is an important strengthening mechanism in Mg alloys, and the influences of precipitates on the details of plastic deformation is a subject of active research. In the current investigation, a commercially available, age hardenable Mg-rare earth alloy WE43 provided in the hot-rolled and aged condition (hereafter, WE-43 T5), with no intermediate solution treatment, is
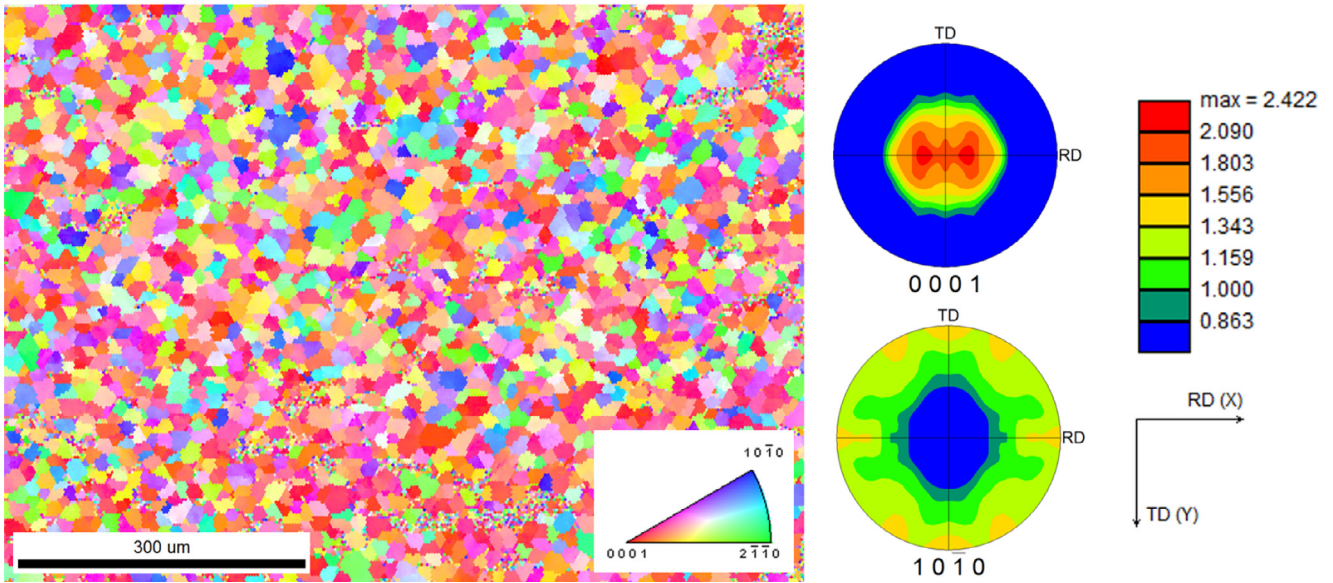
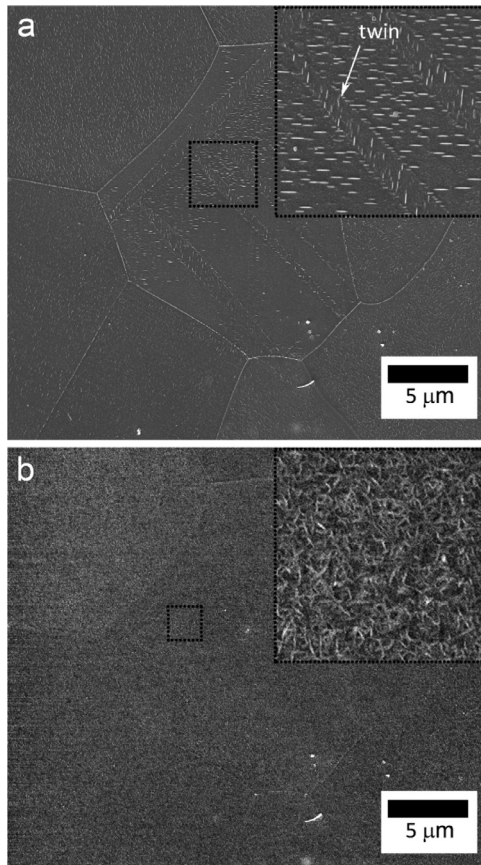**Fig. 1.** EBSD characterization of WE43-T5.

Fig. 2. Polished and etched WE43 Mg in T5 heat treatment condition (WE43-T5). (a) Precipitates formed preferentially along the grain boundaries, making the grain structure more evident. Magnification of a twin in the microstructure shows the re-orientation of the precipitates as a result of the orientation change from twin to parent grain. Precipitates also formed preferentially on the twin boundary. (b) Speckle pattern on same area used for digital image correlation.
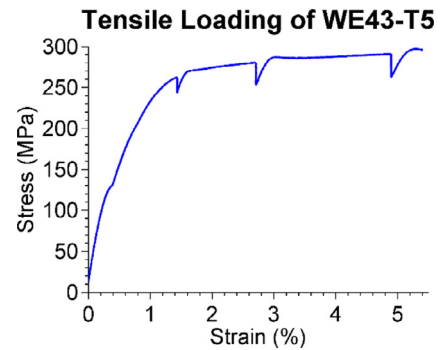

Fig. 3. In-situ stress-strain curve for the tensile loading of WE43-T5. Load was applied along the rolling direction. Strain was measured using an LVDT that was calibrated using the full-field DIC strain data. Stress drops in the stress-strain curve correspond to stress relaxation while SEM images of the surface were captured.

$\beta 1 \rightarrow$ equilibrium β. More recent work suggests that intermediate precipitates of β' and β''' [33] are likely to occur in Mg-Nd-Y alloys [34–37]. As the β', β''' and $\beta 1$ phases form on the prismatic plane, basal dislocation slip is inhibited compared to precipitate plates forming along the {0001} basal plane, as in Mg-Al alloys [33]. As such, the strength of Mg-Y-Nd alloys is improved significantly. For the WE43 alloy investigated in this study, GP Zones, β', β''' were all present in the peak-aged condition [37].

An in-SEM uniaxial tension test was conducted on samples extracted from the WE43-T5 plate to quantify local plastic deformation in fields of view containing several grains, as shown in Figs. 3 and 4. The testing procedure was as follows: first, specimen blanks were machined using wire electro-discharge machining (EDM) to produce flat dogbone-shaped tensile specimens. The samples were designed with the tensile loading direction parallel to the rolling direction (RD). The gauge length was 18 mm, the sample thickness was 2 mm, and the gauge section width was 4.5 mm. The samples were metallographically ground with 600, 800, and 1200 standard ANSI grit silicon carbide paper for thirty seconds at each grit, and then polished with a series of 6 μm, 3 μm, and 1 μm water-based diamond suspensions for five minutes each on medium-napped pads. After each diamond polishing step, the samples were immediately rinsed with soap and water, rinsed with ethanol, and dried with compressed air. Finally,

investigated. Aging was conducted at 204 °C for 48 hours. The precipitation sequence of this alloy has been characterized by TEM in other work [29–32] and proceeds as follows: metastable Guinier–Preston (GP) zones → metastable β'' → metastable β' → metastable
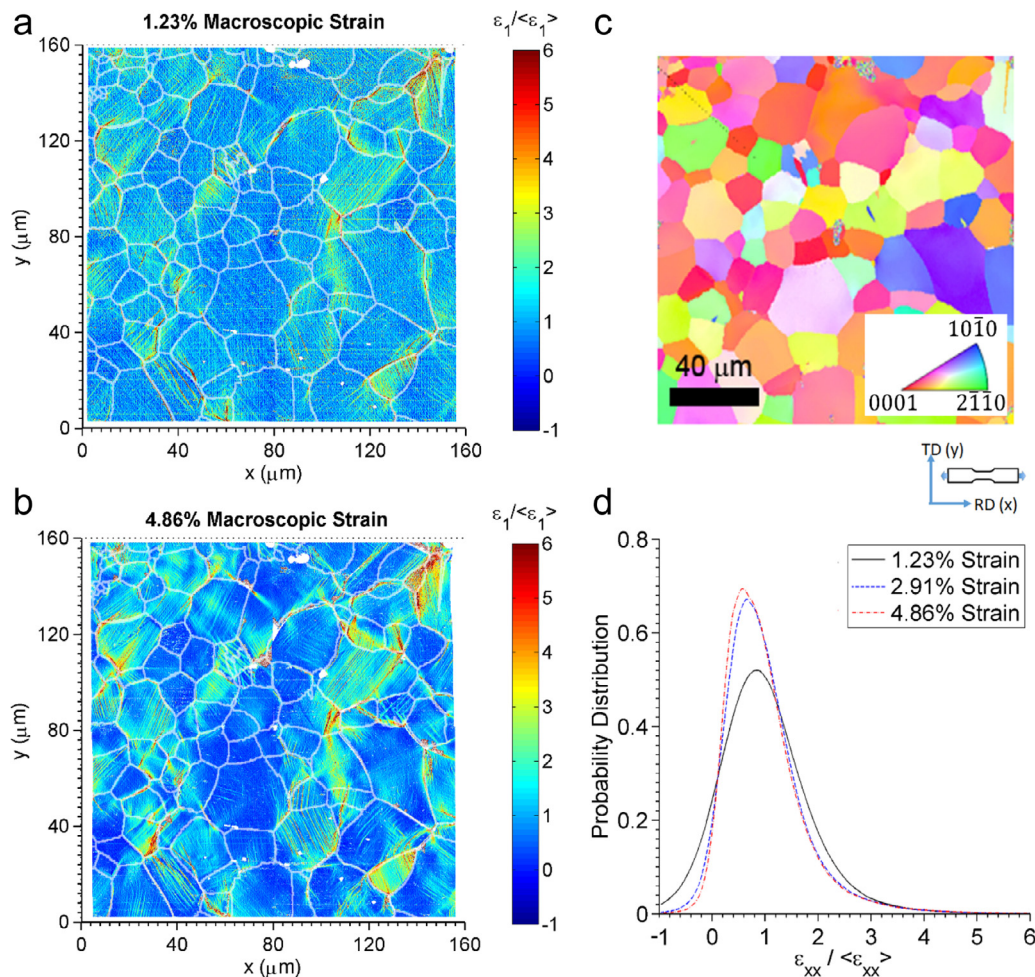
Fig. 4. The normalized maximum principal strain maps on the surface of WE43-T5 at globally-applied uniaxial strains of: (a) 1.23% and (b) 4.86%. (c) The inverse pole figure map shown was measured using EBSD. Strain localizations appeared at the onset of plastic deformation at a globally-applied strain of 1.23%. Comparing images (a) and (b), few new slip traces appeared on the surface with increased macroscopic loading. (d) A probability distribution of the strain field further highlights this; note that the wider distribution at 1.23% global strain is thought to be caused by noise in the SEM speckle pattern images at lower strain levels.

the samples were subjected to a chemo-mechanical polish with a high pH colloidal alumina/colloidal silica mixture for four minutes on a synthetic micro-napped pad, after which they were immediately rinsed with soap and water, rinsed with ethanol, and dried with compressed air. Next, the surface was etched in a solution of 50 ml methanol + 6 ml hydrochloric acid + 4 ml nitric acid for ∼3–5 s, then rinsed with ethanol and blown dry with compressed air. This etchant revealed precipitates on the surface (if any) and greatly improved EBSD results, but did not preferentially etch the grain boundaries. This is important for in-situ testing, where a deep grain boundary etch could act as a stress concentrator and potentially affect the surface strain field.

Platinum fiducial markers were deposited on the specimen surface via focused ion beam. Grain orientations and boundaries were mapped by EBSD. Following EBSD, a speckle pattern for deformation tracking was created as described in the following paragraph, and an in-SEM uniaxial tension or compression test was conducted. In-SEM tensile testing was performed using a Kammrath and Weiss tensile/compression module inside a TESCAN MIRA 3 SEM. The tensile loading was applied using displacement control at 1 μm/s, which corresponds to an approximate strain rate of 6×10^{-4} s^{-1}. Micrographs were taken at various stages of plastic loading, and the displacements were correlated via digital image correlation. SEM images with 8192 by 8192 pixel resolution were taken over a field-of-view of 80 μm by 80 μm. DIC was performed

with a subset size of 35 by 35 pixels and a step size of 2 pixels. Lagrangian strain was calculated from the u and v displacements, and then corrected for the spatial and temporal distortions that arise from SEM imaging using custom codes [38]. The EBSD data was then projected to the distortion-corrected strain data using a projective transformation and 18–20 control points. Because the grain boundaries are visible from the precipitates at this length scale, triple points were used in addition to fiducial markers as control points for the mapping.

Two methods were utilized for creating a suitable speckle pattern for microscale DIC on magnesium alloys. Since magnesium alloys are corrosion-susceptible, sample preparation techniques designed to prevent corrosion were required. The first method involves the self-assembly of gold nanoparticles and is detailed in [28]. As explained in [28], the advantage of this technique was an easily controlled speckle size that can be tailored the exact field of view being investigated. A disadvantage is that the self-assembly process has a relatively low yield on Mg and its alloys, and may need to be repeated several times to get a working pattern. The second method, which was developed for the experiments presented in this paper, was to use a strong alkaline immersion technique to grow thin needle structures on the surface. After EBSD, the surface was cleaned of hydrocarbon contamination using either an oxygen plasma or by re-polishing using a high pH colloidal alumina/colloidal silica mixture for 30 s. Etchants
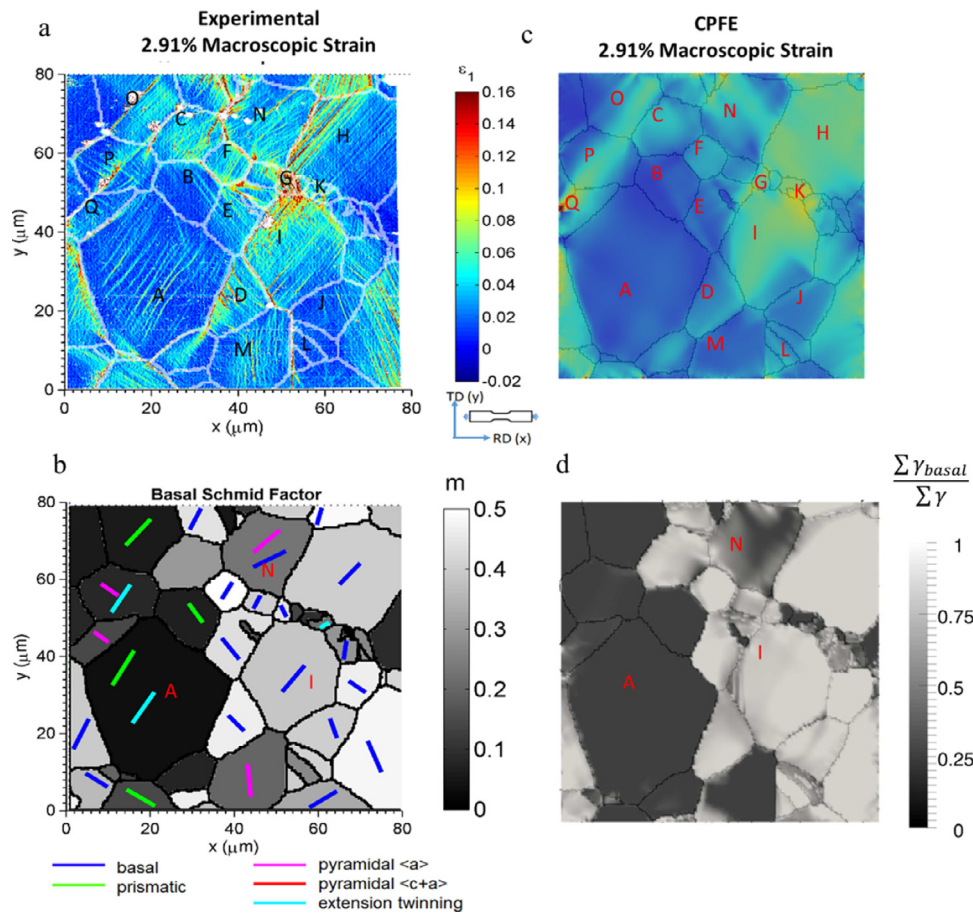
Fig. 5. Slip traces in the strain map of (a) were identified using EBSD data as shown in (b). Basal and non-basal systems were activated, with basal slip occurring on grains with high nominal Schmid factors for basal slip. (c) Comparison of predicted slip systems from CPFE model at the same global strain level as the experimentally measured strain field. (d) The CPFE prediction of the relative activity of basal slip.

remove too much of the sample surface and should not be used for cleaning. Next, the sample was immersed in in 1 M NaOH at 50 °C for 1 h, rinsed with water for 30 s, and then blown dry using compressed air. The thin needles formed from this alkaline immersion, and an example of this pattern is shown in Fig. 2(b) for the tensile testing; the advantage of this technique is high resolution and repeatability; however, as this is a natural growth procedure versus the application of pre-fabricated nanoparticles, the field of view is limited and tied to the needle growth size.

2.2. Uniaxial compression

Compression tests were performed on flat dog bone-shaped test samples with gage dimensions of 10 mm x 3.5 mm x 3.5 mm. The sample was machined by wire EDM, polished and etched, and characterized by EBSD with a 0.5 μm step size to determine crystal orientation. After EBSD, the sample was patterned with gold nanoparticles with 40 nm nominal diameter for digital image correlation following the nanoparticle method described above, with the addition of NaOH to the Au NP suspension in order to reduce corrosion. In-SEM compression testing was performed using a Kammrath and Weiss tensile/compression module inside a TESCAN MIRA 3 SEM. Compression loading was applied using displacement control at 2 μm/s, which corresponded to an approximate strain rate of 2×10^{-4} s^{-1}. The test was paused periodically to capture images, and was terminated at ~5% global compressive strain. SEM images with 4096 by 4096 pixel resolution were taken over a field-of-view of 45 μm by 45 μm. Thirty-six FOVs were monitored. DIC

was performed with a subset size of 27 by 27 pixels and a step size of 3 pixels.

3. Experimental results and analysis

3.1. Uniaxial tension

A sample was loaded in tension parallel to the rolling direction, with images taken at three main strain intervals. Fig. 3 shows the uniaxial tensile stress-strain curve. Stress relaxation occurred while the test was paused at three strain levels in order to capture SEM images of the surface. Fig. 4 shows the normalized strain fields at the two loading steps evident in Fig. 3. Normalized strain is the local strain divided by the average macroscopic strain, where for example, a value of 2 denotes that the localized strain is twice the average strain. Four 80 μm by 80 μm view fields were stitched together to examine plastic behavior over a larger area, and grain boundaries were overlaid onto the strain fields.

Despite displaying substantial strain heterogeneity, there was little change in the locations of high strain after yielding. Strain heterogeneity remained fairly constant with increased global loading, where localized strain developed early in plastic deformation and did not change spatially with increased plastic straining. Fig. 4(d) shows the probability distribution of strain as a function of increased loading. The distribution did not change significantly between the second and third strain step. The distribution was wider for the first strain step, but it was suspected that this
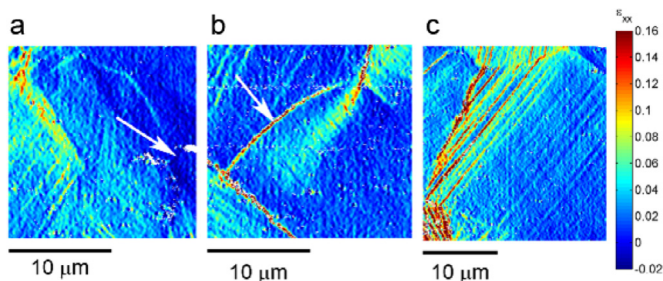
Fig. 6. High magnification detailed images of the ε_{xx} strain field shown in Fig. 3. (A) The appearance of a localized region of compressive strain (see arrow) suggests large deviated stress states from uniform uniaxial tension (the macroscopic stress state). (B) Diffuse strain not associated strongly with individual slip traces. Also shown is high strain along a grain boundary (see arrow). (C) The magnitude of strain from individual slip traces may vary widely across a grain. Tensile load was applied in the *x*-direction.

widening is due to SEM-induced noise at this low strain level and not from material behavior.

The strain from individual slip traces was resolved and quantified, as evident in Fig. 5(a), which has not been previously reported for magnesium. Examples of interesting features on these strain maps are shown at higher magnification in Fig. 6. This allows a unique perspective on the characterization of independent slip systems during tensile loading. Interestingly, Fig. 6(a) shows local compressive (ε_{xx}) strains in a sample that was loaded macroscopically in tension. The direction of loading was in the xx direction. This indicates that the local stress state may deviate considerably from uniform uniaxial tension to accommodate nearby strain. Regions of diffuse strain not associated with distinct slip traces were also observed, as shown in Fig. 6(b). This may be caused by stresses from neighboring localized regions of high strain (e.g. an activated slip system or grain boundary strain) including subsurface features. These stresses may be caused by twinning, microcracking, or highly deformed neighboring grains that result in plastic deformation similar to the plastic zone in front of a crack tip. Additionally, it was found that the slip systems activated in an individual grain displayed a wide range of strain magnitudes, as shown with an example in Fig. 6(c). Traditional slip trace analysis shows the activation of specific slip systems, but does not quantify the strain associated with these slip traces. It was shown here that when slip is activated within a grain, certain traces carry higher strain than others. Apparently identical slip modes inside a grain

can produce axial strains in the direction of loading that vary by a factor of four or more, as shown in Fig. 6(c).

By combining EBSD and full-field strain data, it was possible to identify the active slip systems by slip trace analysis of the surface. Basal slip was expected to dominate due to its low CRSS compared to the other systems. Fig. 5(a) shows the ε_1 strain field showing the active slip systems on the surface, and Fig. 5(b) shows the plot of nominal Schmid factor for basal slip, along with apparent slip system associated with the slip traces that were observed on the surface. Nominal Schmid factor refers to the Schmid factor calculated by standard EBSD software assuming that the loading axes is parallel with the x-axis. It does not account for the reorientation of stresses locally due to constraint of surrounding grains and grain neighborhoods, here-in referred to as local Schmid Factors as discussed in the PRISMS-Plasticity CPFE section. Grains with high nominal basal Schmid factors tended to deform via basal slip, as seen in 5(b). In grains with lower nominal basal Schmid factors, alternate slip systems were observed and this also roughly correlated with the nominal Schmid Factor for the appropriate nonbasal slip mode as shown in Fig. 7(a) and 10. Slip trace analysis relies on a knowledge of the geometry of the slip system and its intersection with the surface; thus, in some situations there was ambiguity in which slip system was operative due to the nearly identical intersection angles. The combination of CPFE (shown in Fig. 5(c), (d) and 7(b), and described in Section 4.1 below) and this experimental data helped clarify ambiguous slip system traces.

The apparent active slip systems were identified and analyzed in all twelve 80 μm by 80 μm fields. Among a total of 294 grains, 123 grains exhibited identifiable slip or twinning activity. For the remainder of the grains, either slip traces or twinning were not clear enough to be identified, and only diffuse strain was observed, or the grain did not show significant evidence of deformation. In most grains, only one set of slip traces or twinning areas was observed. Fig. 7(a) shows the number of activations of different types of slip or twinning activity (a set of slip traces of the same slip system in one grain was counted only once) and their Schmid factors. It was found that basal slip was frequently activated during tensile loading, as is expected with magnesium alloys due to the lower CRSS. It was also observed that non-basal slip was activated to a significant degree as well. Extension twinning occurred less frequently.

Grains with nominal basal Schmid factors of >0.3 were observed to deform on basal slip planes about 50% of the time, which is consistent with the expectation from Schmid's Law. About 50%
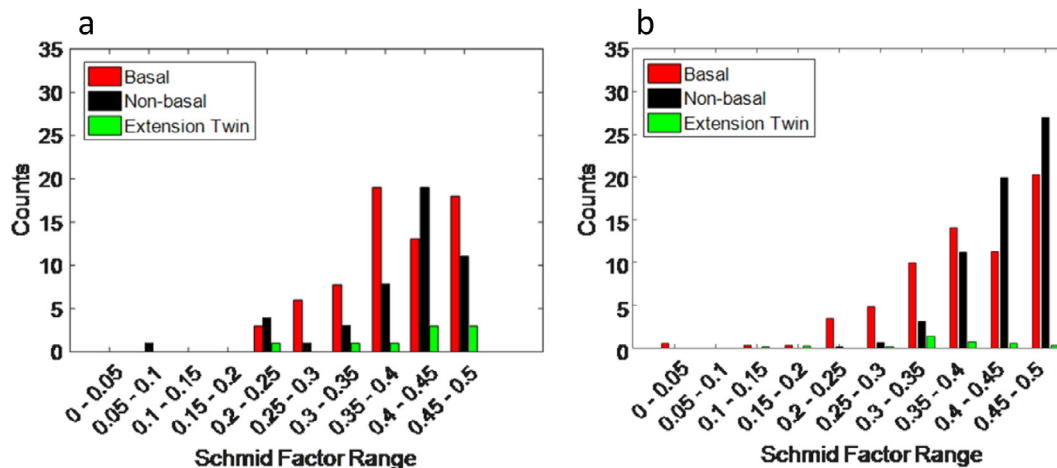

Fig. 7. Distribution of the active slip/twinning systems with respect to their nominal Schmid factors for tensile test at 4.86% globally-applied strain for (a) DIC data (b) CPFE data. A set of slip traces on the same slip system in one grain was counted only once.
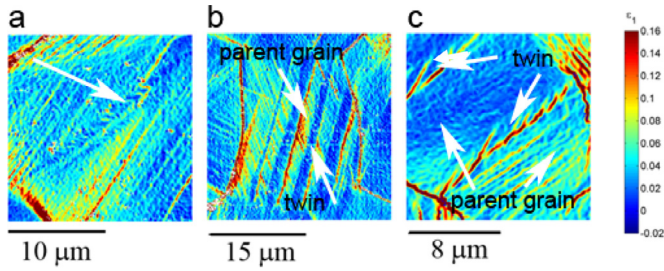
Fig. 8. Interaction of preexisting twins with basal slip processes. (A) Basal slip redirects through a preexisting twin with a significant shift in direction, shown with an arrow. (B) Preexisting twins resists deformation, and high strain occurs along the twin boundaries. (C) Preexisting twins deform via pyramidal $<c+a>$ slip while the parent grain deforms via basal slip, and high strain occurs on the twin boundary.

were activated to varying extents, with prismatic slip and twinning occurring more frequently. Even though a large number of grains had high nominal Schmid factors for non-basal deformation modes, and thus were oriented favorably for these systems to activate, the corresponding slip systems were not always observed. In fact, often the non-basal variant that activated did not have the largest nominal Schmid factor within its family of symmetric slip planes. This presumably relates to the higher CRSS of the particular non-basal slip mode and activation of these non-basal systems was not determined solely by the macroscopic loading state. In addition to CRSS differences, slip transfer or constraint from neighboring grains including adjacent subsurface grains also can play a role. Another mechanism similar to the diffuse strain mechanism exhibited in Fig. 6(b) is one in which the local stress state (e.g. the local Schmid Factor) varies significantly from the macroscopic stress state (which was used to calculate the nominal Schmid factors) due to the impact of high strain localizations in neighboring grains including subsurface grains. The importance of these factors is confirmed using the crystal plasticity finite element simulations described in the next section.

Tension twins existed in the undeformed microstructure as a result of the hot rolling process, and are not affected by
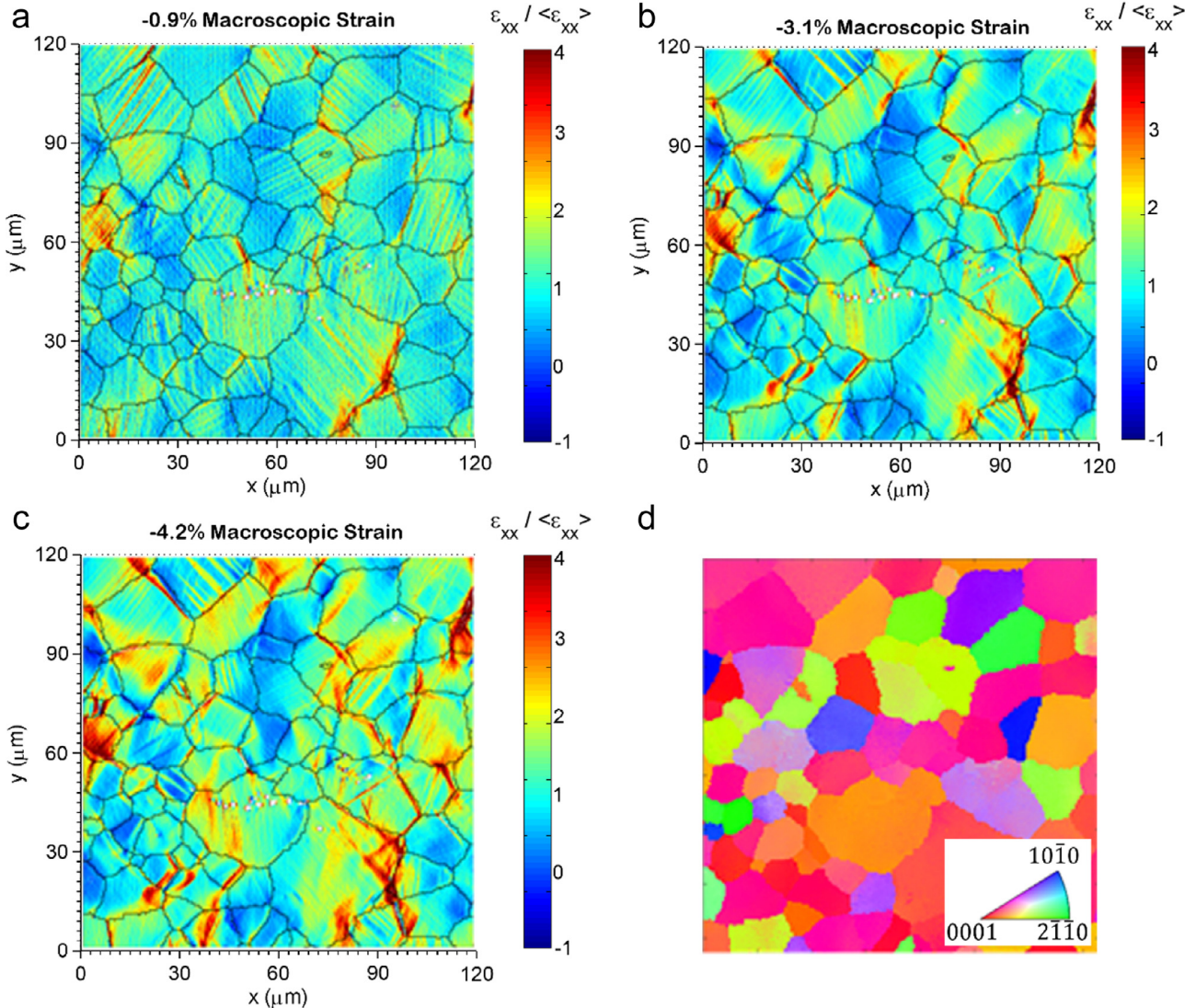
of grains with a basal Schmid factor >0.3 did not deform via basal slip; it is unknown why basal slip was not activated in these grains.

Similar to basal slip, there was a correlation between activation and a high nominal Schmid factor for a specific slip system in the non-basal systems. All four of the non-basal systems

Fig. 9. The normalized tensile strain (E_{xx}) maps on the surface of WE43-T5 at three different global strain levels during *in-situ* compression test: (a) -0.9% strain, (b) -3.1% strain and (c) -4.2% strain. (D) Inverse pole figure in the undeformed state. Slip traces were observed at the onset of plastic deformation at global compressive strain of 0.9%. Twinning was observed with increasing global strain. Selected twinned regions were highlighted with circles in the images.

subsequent low temperature aging at 204 °C. The interaction of these preexisting twins with the neighboring parent grain is highlighted in the strain fields shown in Fig. 8. Evidence of slip transfer via a significant redirection of the slip plane was shown in in Fig. 8(a), where basal slip traces show a jog through the twin, shown with an arrow. Some twins were entirely resistant to further deformation in Fig. 8(b), and exhibit high strain along the twin boundary, possibly due to dislocation pileup similar to a grain boundary. Fig. 8(c) showed a twin deforming by a non-basal slip system, while the parent grain deformed predominately by basal slip, and high strain occurred on the twin boundary in this instance as well.

3.2. Uniaxial compression

Compression testing was performed *in-situ* along the rolling direction of the test specimens. The compression axis was parallel to the x-direction. Fig. 9 shows the strain map of an area within the center of the gage section at different global strain levels. The development of heterogeneous strain shared similarities with those observed during tension, i.e., strain localization was observed at the onset of global yielding, and the locations of high strain remained fairly constant with increasing global strain. Both slip and twinning were active. As shown in Fig. 9(a), which corresponds to approximately 0.9% of global compressive strain, slip traces were observed in a large number of grains. Some regions, especially near certain grain boundaries, exhibited much higher localized strains compared to the other regions. As global compressive loading increased, both the number of slip traces and the intensity of strain on the slip traces increased, as shown in Fig. 9(b) and (c). (Note: positive strains are in compression in these images). Twinning was also observed, examples of which are indicated by black circles on the map in Fig. 9(b) and (c). At higher strain, both the area and number of twins increased. However, because the twin shear is a fixed value (for Mg it is 12.9% for extension twinning), the measured strain in the twinned region did not change significantly; small changes in the experimental data are attributed to noise and sample or grain rotations.

Microscale deformation mechanisms under global compression were dominated by basal slip and extension twinning. Activation of basal slip and extension twinning was strongly correlated with Schmid factor, where a high probability of activation was associated with increasing Schmid factor. The analyzed area contained 340 grains, among which 145 grains exhibited identifiable slip or twinning activity. For the remainder of the grains, slip traces or twinning were not clear enough to be identified, and only diffuse strain was observed. In most grains, only one set of slip traces or twinning areas was observed. Trace analysis was performed to identify the active slip/twinning systems during compressive loading. Fig. 10 shows the number of activations of different types of slip or twinning activity (a set of slip traces of the same slip system in one grain was counted only once) and their Schmid factors. It was found that unlike tension, deformation was dominated by basal slip and extension twinning during compressive loading, and the activation of other non-basal slip systems was very low (i.e., not high enough to generate macroscopically identifiable slip traces on the sample surface).

Apart from extensive twinning activity, an interesting and related mechanism was the detwinning of pre-existing twins in the sample during compressive loading. As illustrated by the IPF map in Fig. 11(e), several pre-existing twins were observed in the undeformed sample. During deformation, as shown in Fig. 11(a) and (b), compressive strain developed in these pre-twinned regions, evolving gradually from the twin boundary to the interior of the twins; therefore, during compression, these twins tended to reorient back to the parent grain orientation. This can be inferred by the EBSD
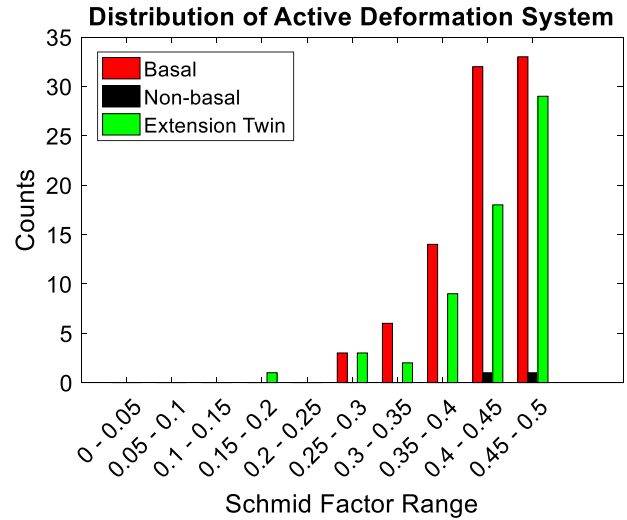

Fig. 10. Distribution of the active slip/twinning systems with respect to their nominal Schmid factors under compressive loading at -4.2% global strain level. Unlike tension, deformation was dominated by basal slip and extension twinning during compressive loading, and the activation of other non-basal slip systems was low.

data, which shows that for these pre-existing twins, deformation by extension twinning led to extension along the *c*-axis (sample thickness) direction, resulting in compression in the sample longitudinal direction. These experimental results will be compared with the CPFE simulations in the next section.

4. Comparison with CPFE models

The DIC results were compared with crystal plasticity finite element (CPFE) simulations produced using the PRISMS-Plasticity code. The objective was to test the CPFE model compared to DIC data, identify Schmid factor variations due to the effects of neighboring grains, and to computationally (rather than geometrically) differentiate the slip traces observed in the DIC data into various slip and twin systems. The 3-D crystal plasticity finite element (CPFE) PRISMS-Plasticity code is open source [1,2] and is based on a fully implicit implementation of an elastoplastic single crystal model [14–17]. Crystallographic slip, twinning and re-orientation of crystals are assumed to be the primary mechanisms of plastic deformation. For a material with $\alpha = 1, \ldots, N$ slip/twin systems; the resistances s^{α} (t) > 0 offered by the slip/twin systems at time t depends on the plastic shearing rates t on systems α through a hardening law:

$$\dot{s}^{\alpha} = \sum_{\beta=1}^{N} h^{\alpha\beta} \left| \dot{\gamma}^{\beta} \right|, \quad \text{where } s^{\alpha}(t=0) = s_o^{\alpha}$$

$$h^{\alpha\beta} = h_0{}^{\beta} (q + (1-q)\delta^{\alpha\beta}) \left(1 - \frac{s^{\beta}}{s_{sat}^{\beta}} \right) \quad \text{(no sum on } \beta)$$

Where, the slip system hardening term ($h^{\alpha\beta}$) includes latent hardening through parameter q, taken to be 1 for coplanar slip systems and 1.4 for non-coplanar slip systems [18]. The parameter s_o^{α} is the initial critical resolved shear stress for system α, and $h_0{}^{\beta}$ and s_{sat}^{β} are the hardening rate and saturation resistance of slip system β respectively. These three parameters are calibrated for each slip system such that the CPFE model predicts the experimental stress-strain response under different deformation modes. Other aspects of the model including elastoplastic decomposition, flow rule and constitutive update algorithm are detailed in [1].
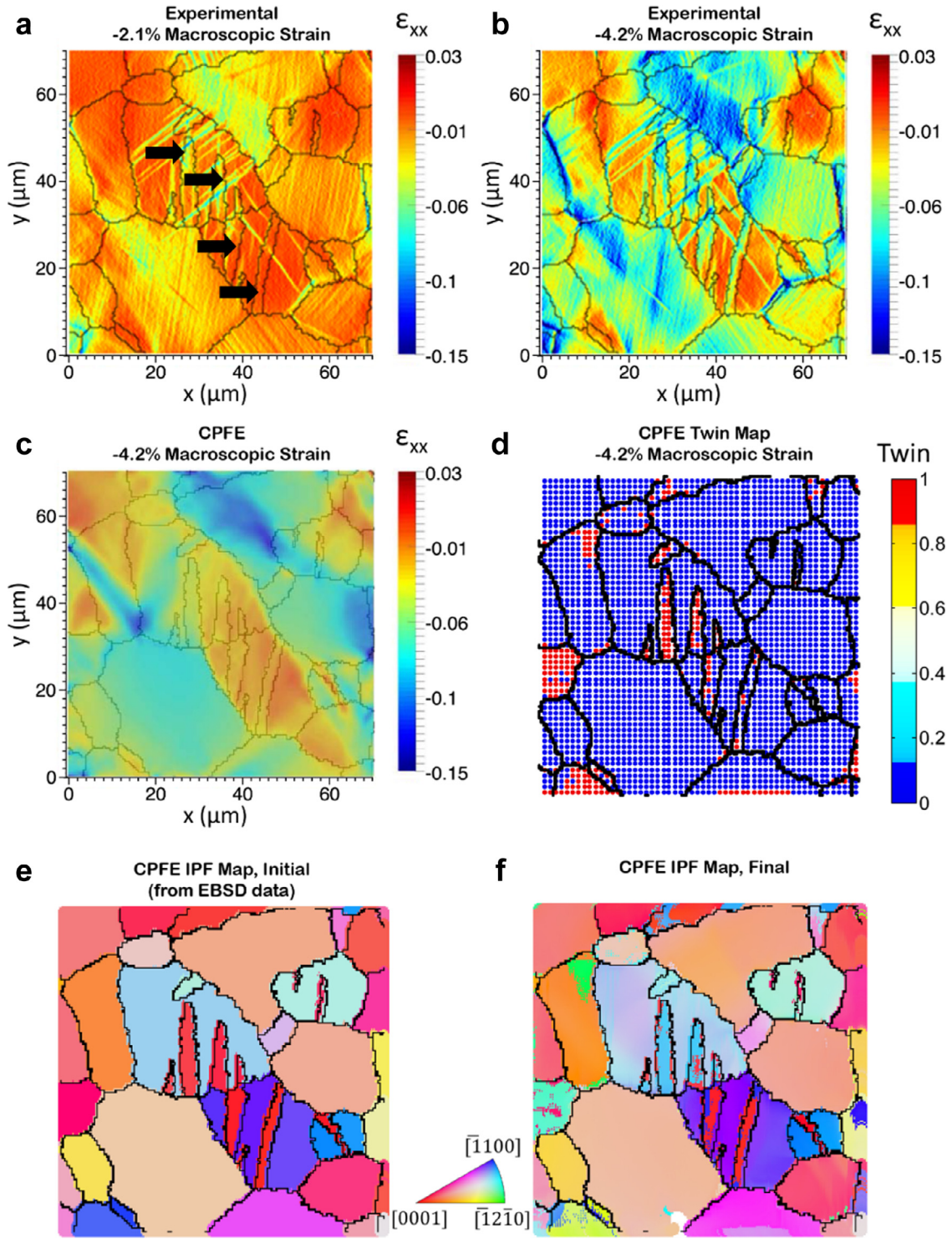
Fig. 11. (a) ε_{xx} strain map at 2.1% global compressive strain, and (b) 4.2% global compressive strain. (c) Comparison of the strain field using CPFE during compression test at 4.2% strain. (d) The location of twins (due to detwinning) as predicted from CPFE model are also shown (e) IPF map of a region where detwinning of pre-existing twins occurred during compression. (f)) The final microstructure as predicted by CPFE showing the detwinning.

The volume fraction associated with each twinning system, g^{n,t_i} increases with loading, and the fraction at quadrature point n at any given loading step is given by

$$g^{n,t_i} = \sum_{steps} \Delta g^{n,t_i} \quad \text{where } \Delta g^{n,t_i} = \frac{\Delta \gamma^{n,t_i}}{S}$$

Where t_i denotes the twinning system i, S is the character-istic shear strain of the twin and $\Delta \gamma^{n,t_i}$ is the shear increment

of the twin system at the loading step. For pure Magnesium and Mg-alloys, S = 0.129. The total fraction of twins is calculated lo-cally at each quadrature point. If it exceeds a critical value (i.e. $\sum_i g^{n,t_i} > F_T$), the quadrature point is reoriented. F_T is taken to be 0.25 based on the predominant twin reorientation (PTR) scheme in [39]. The crystal elastic parameters for Mg alloy are taken to be: $C_{11} = 59.3$, $C_{12} = 25.7$, $C_{13} = 21.4$, $C_{33} = 61.5$ and $C_{55} = 16.4$ (in MPa) [40].
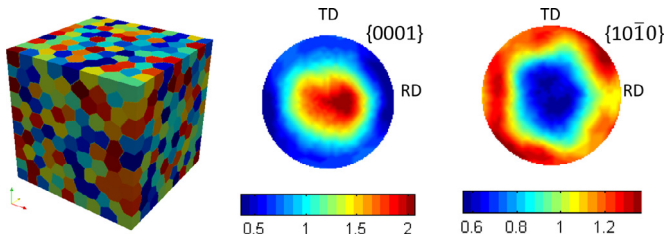
Fig. 12. Polycrystal RVE of 1000 grains generated with centroidal voronoi tessellation and the initial weak basal texture associated with grains in the RVE.
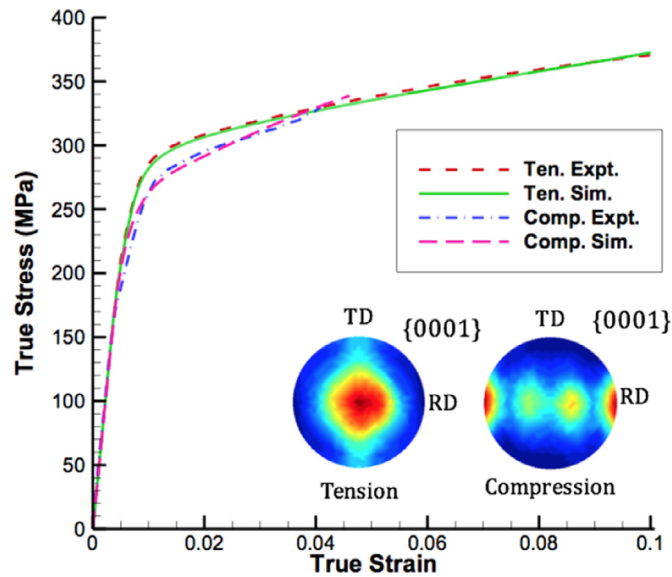

Fig. 13. Experimental and simulated stress-strain curves for tension and compression. CPFE simulations of the {0001} Simulated pole figures after tension and compression at final strain are shown (inset).

Table 1
Hardening parameters for simulating stress-strain curves.

Mode	s_0^α (MPa)	h_0 (MPa)	s_{sat} (MPa)
Basal $<a>$	76.0	225.6	248.7
Prism $<a>$	163.2	124.9	356.3
Pyram $<a>$	160.3	120.2	347.8
Pyram $<c + a>$	187.4	237.9	350.4
Twin $<c + a>$	116.4	105.6	238.3

Table 2
Comparison of CRSS of individual modes for T5 temper used in this study compared with those from Stanford et al [42] and Bhattacharya et al. [43].

Mode	$s_{0\ CPFE}^\alpha$ (MPa)	$s_{0\ Stanford}^\alpha$ (MPa)	$s_{0\ EPSC}^\alpha$ (MPa)
Basal $<a>$	76.0	68	68
Prism $<a>$	163.2	179	145
Pyram $<a>$	160.3	-	-
Pyram $<c + a>$	187.4	273	210
Twin $<c + a>$	116.4	106	130

texture is a weak basal texture, twinning is observed primarily during compression loading.

Initial strengthening due to precipitates is included in the CRSS of slip systems since they are calibrated against the measured yield strength of the specimens. The strains simulated are low (up to 5%); and hardening due to precipitate interactions is not expected to be significant enough to be accounted for explicitly. Instead, hardening parameters are chosen such that it predicts the experimental stress-strain response under tension and compression modes as shown in Fig. 13.

Using the optimized CRSS and hardening parameters shown in Table 1, the relative activity of different slip systems predicted by CPFE during simulations of tension and compression loading are shown in Fig. 14. Under both tension and compression, basal slip is the most active mechanism. Under tension the $< c >$ poles scatter minimally normal to the loading axis (along lateral direction) as expected due to low twinning and predominance of basal slip shown in Fig. 13 (inset). While pyramidal $<a>$ slip is the second most active mechanism in tension, during compression along RD, pyramidal $<c + a>$ and twin-induced reorientation mechanisms are second most active. The $< c >$ axis realigns in the compression direction due to twinning. Therefore, these mechanisms have the tendency to rotate the crystallographic lattice towards the RD, as seen in the simulated 0001 poles shown in Fig. 13 (inset).

The calibrated hardening parameters employed for the basal, prismatic, pyramidal and twin systems are tabulated in Table 1. The critical resolved shear stresses are compared to those published in literature for this alloy and shown in Table 2. The basal slip resistance at 76.0 MPa is higher than in [42,43], while the twin resistance is lower. The differences between the models are within the deviations expected due to differences in the initial grain sizes, heat treatment, cold work and texture of the alloy and the differences in the modeling approach. For example, Refs [42,43] did not employ pyramidal $<a>$ mechanism, but it is included here since some of the slip traces observed were close to the pyramidal $<a>$ plane.

4.1. Calibration of CPFE model parameters

The experimental specimen that was used to generate the tension and compression response had a weak basal texture. A 3D representative volume element (RVE) with 1000 grains was constructed with the open-source software package Neper [15,41]. The RVE with centroidal voronoi tessellation was generated using Lloyd's algorithm. As grain size effects were not considered in the current computation, centroidal voronoi tessellation ensured well-shaped and uniformly sized convex cells. The presence of a larger number of grains in the RVE allowed it to map to the experimental texture accurately. The RVE and its simulated texture is shown in Fig. 12.

The RVE was subjected to simple tension and simple compression boundary conditions. The CP parameters were calibrated by a gradient optimization approach starting from the parameters of WE43 T5 published in literature [42]. The goal was to minimize the L2 norm of the error between the experimental stress-strain curves and the CPFE homogenized curves for tension and compression tests simultaneously. The crystal plasticity tensile CRSS and hardening coefficients were fit at 10% true strain and the compression data was fit at 4% true strain, as shown in Fig. 13. The asymmetry of the tension and compression stress-strain curve occurred due to the directionality of tensile-twins. Unlike the slip systems for which slip can occur along both the positive and negative directions, twinning is polar in nature due to the underlying atomic arrangement. We consider only extension-twins for this alloy, therefore twinning occurs with extension along $<c>$ direction. Since the

4.2. CPFE simulations with 2-D microstructure

The comparison with SEM-DIC experiments was performed by setting up a boundary value problem using the EBSD image of the microstructure within the DIC window as the simulation microstructure. The displacement fields in the x and y direction along the boundary of the microstructure were obtained from the SEM-DIC experiment. The measurements are made on the surface of the sample, which is traction-free, and therefore a plane-stress
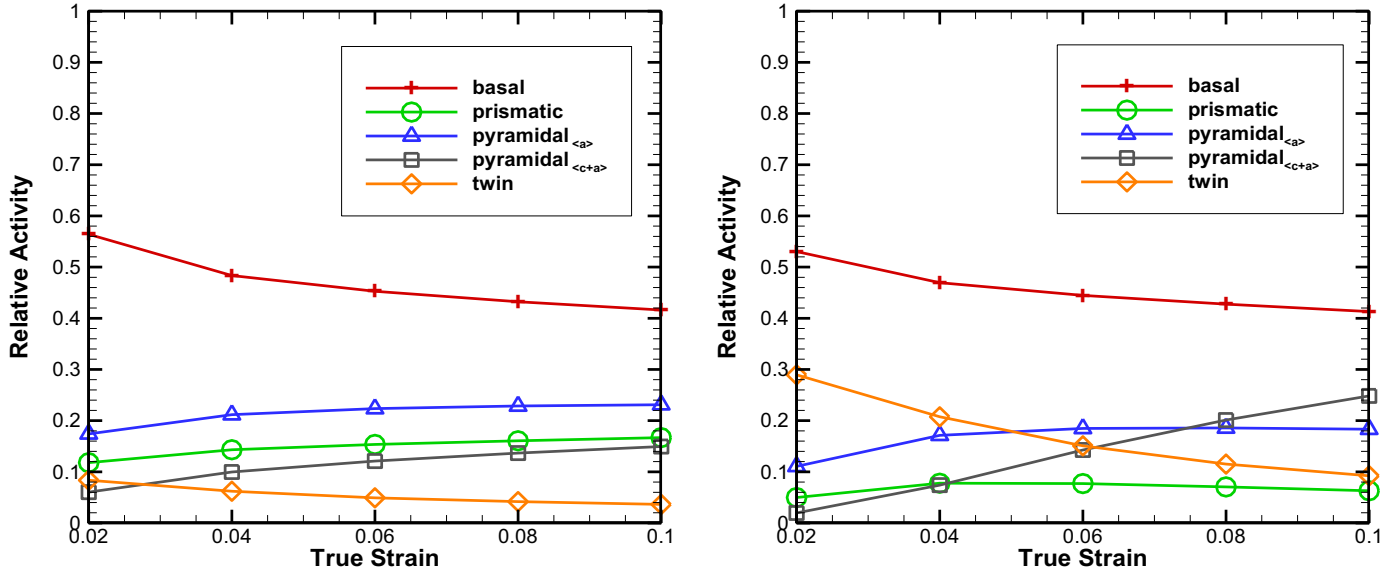
Fig. 14. Relative activity of slip modes predicted by the CPFE simulation during (a) tension and (b) compression along the RD.

Table 3
Comparison of mean axial strain ($\bar{E}_{xx}$) for the labeled grains between SEM-DIC experiments and CPFE simulations.

Grain ID	Schmid factor (m)	$\bar{E}_{xx}$ (SEM-DIC)	$\bar{E}_{xx}$ (CPFE)
A	0.02	0.018	0.021
B	0.05	0.020	0.020
C	0.34	0.040	0.021
D	0.46	0.044	0.022
E	0.43	0.035	0.030
F	0.50	0.044	0.023
G	0.44	0.102	0.043
H	0.37	0.032	0.046
I	0.38	0.046	0.037
J	0.39	0.017	0.049
K	0.24	0.038	0.041
L	0.30	0.016	0.045
M	0.20	0.025	0.027
N	0.24	0.038	0.041
O	0.05	0.031	0.022
P	0.06	0.022	0.027
Q	0.18	0.039	0.049

assumption is made while setting up the simulation. The slip and twin systems are three-dimensional and the algorithm to solve for the shear strains and stresses in the slip systems proceeds from a 3-D deformation gradient. Therefore, it is not possible to set up an explicit plane-stress problem similar to 2-D elasticity. Instead, the problem is set-up in 3-D with a plate of very small thickness. A thickness to length ratio (t/l) of 0.1 was used for all the simulations. Since no variation of variables 'u' and 'v' was expected in the z-direction, a single layer of elements was assumed in the z-direction along with a 150 × 150 mesh.

The CPFE predictions of the strains in the x-direction in a tension test (loaded in the x-direction) are plotted alongside the DIC strain map in Fig. 5(c). The mean Lagrangian strain ($\bar{E}_{xx}$) in the loading direction for the grains labeled in Fig. 5 (a,c) is tabulated in Table 3. A direct comparison reveals that overall strain distribution was captured reasonably well in the CPFE simulations, with grains with low strains (A,B,E,P) correctly predicted. Strains in grains with moderate strain (I,M,N,O,Q) were also well predicted. There are a few discrepancies. A region in the DIC image has high strains (G) and corresponds to a cluster of small grains. This could arise due to Hall–Petch or the increased localization of strains at the grain

boundary, neither of which are included in the FEM simulation. The strains in that region are lower in the CPFE simulation, and the grains surrounding that region take up more strains (K,H) to achieve overall equilibrium. Similarly, grain boundary activity can be seen in grains marked C,D and F; these grains show moderately high strains in the DIC image as compared to the CPFE simulations. The surrounding (A, M, N, P and Q) take up more strains in CPFE simulation as compared to the DIC image as can be seen from Table 3. There are a small number of grains where strains are not well predicted, such as J and L. Note that we have made no attempt to calibrate the CPFE model based on the DIC strain maps, but rather the CPFE model parameters were calibrated based on the macroscopic stress-strain response. In this light, the DIC strain maps predicted by CPFE are encouraging. Also, CPFE does not predict the shear localizations that are seen in the DIC maps. These fine slip bands occur naturally in experiments while special techniques (bifurcation analysis [44]) are needed in CPFE to capture such phenomena.

A comparison of SEM-DIC and CPFE for the compression case, where significantly more twinning is observed, is shown in Fig. 11. A direct comparison of the strain map is shown in Fig. 11(b,c) at an applied strain of 4.2%. As is the case of tension test, the overall strain prediction is satisfactory, while fine strain localizations are not captured. We primarily focus on the twinning process during compression. Fig. 11(d) shows the twin activity in various grains. Prior to compressive straining, twins were present in the starting structure as shown by arrows in Fig. 11(a). These pre-existing twins were presumably formed during the hot rolling process. During compression, we observe that the deformation is accommodated by recovering these pre-existing twins (in the form of detwinning) as seen from the inverse pole figures in (e,f). As can be noted from Fig. 13, the initial yield strength in compression was approximately 10% lower than that in tension. This can be attributed to the activation of extension twinning in compression. At the macroscopic level this can be seen as an increase in predicted twin activity (Fig. 14b). At the microscopic level this can be related to both the formation of deformation twins shown in Fig. 9(b) and (d) or to the detwinning process shown in Fig. 11(e) and 11(f).

In the following, we compare the slip systems predicted by CPFE with the DIC slip trace analysis to further validate the CPFE simulations. We primarily focus on the tension test results in Fig. 5. The CPFE simulations can be used to identify effects that arise
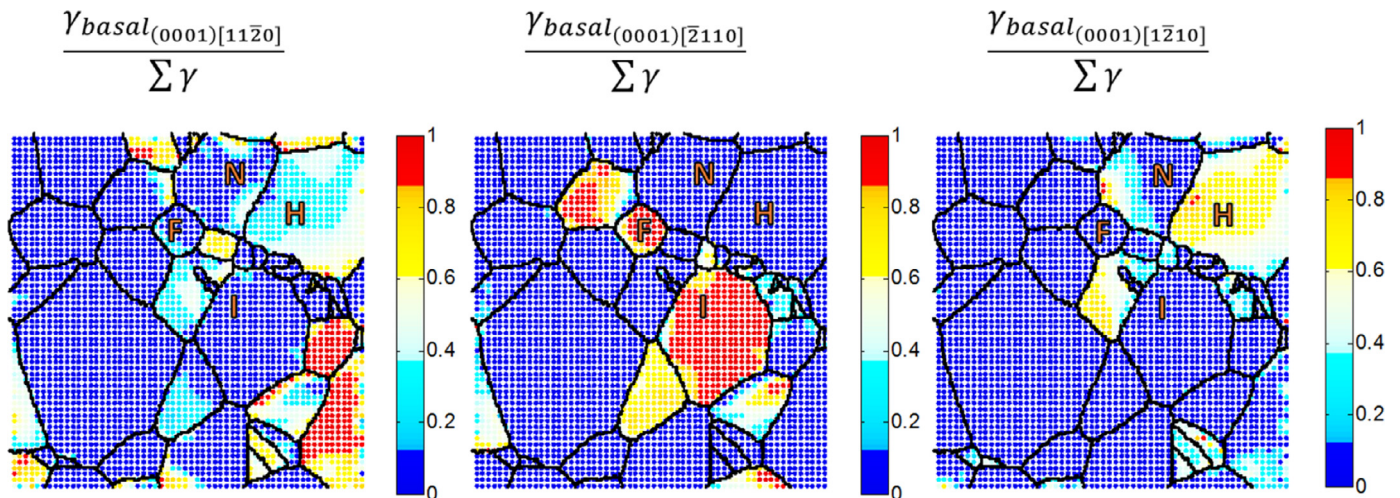
$$\frac{\gamma basal_{(0001)[11\bar{2}0]}}{\sum \gamma} \qquad \frac{\gamma basal_{(0001)[\bar{2}110]}}{\sum \gamma} \qquad \frac{\gamma basal_{(0001)[1\bar{2}10]}}{\sum \gamma}$$

Fig. 15. The relative activity of the three basal slip systems are compared using quadrature point data from the CPFE simulation.

due to the strain accommodation by neighboring grains to maintain overall equilibrium. These local Schmid Factors provide superior predictions of deformation compared to the nominal Schmid Factors determined from EBSD software. In Fig. 5(b), the DIC traces that are identified are shown superposed on map showing the nominal basal Schmid factors for the associated grains. In Fig. 5(d), the CPFE prediction of the relative activity of basal slip is shown. The relative activity shows the fraction of the total plastic shear carried by the three basal slip systems. In all the grains with high basal activity (lighter grains) predicted by the CPFE simulation (e.g., grain marked I), basal traces were also observed in the DIC experiment as indicated in Fig. 5(c). The darker regions correspond to regions of relatively low basal activity. These regions in Fig. 5(d) (e.g., grain marked A) correspond well to grains with low nominal basal Schmid factor and low basal slip activity as determined by the SEM-DIC traces in Fig. 5(b). In such grains, other slip systems (mainly prismatic and pyramidal $<a>$ slip) are active as seen from the traces shown in Fig. 5(b). Some grains show regions of both high and low basal activity that are not necessarily associated with an appropriately high nominal Schmid factor for the operating slip system. One example is grain marked N in Fig. 5(b,d). In this grain, which had a basal Schmid factor of 0.24 some parts of the grain deform predominantly by basal slip while others by pyramidal $<a>$ as indicated in the DIC trace analysis. We attribute this to strain accommodation related to straining in the adjacent subsurface grains. The pyramidal $<a>$ activity of the grain N can be seen in Fig. 16.

CPFE simulations can be used to differentiate between the three types of basal slip systems that correspond to the same basal slip trace. In Fig. 15, the relative activity of the three basal slip systems are compared using quadrature point data. Review of Fig. 5(b), shows that all grains with high basal activity have a basal Schmid factor greater than 0.3. In the grain marked N, where both pyramidal $<a>$ and basal slip systems are active the basal Schmid factor is 0.24. In some grains, two basal slip systems are simultaneously active (grain marked H). In the grain marked N, some parts of the grain have slip system 1 active, while others have slip system 3 active. Most other grains have only one basal system active (e.g. grains marked I,F) during early deformation.

In Fig. 16, SEM-DIC slip trace analysis results are shown for grains in which non-basal slip traces were observed. These are compared with the slip activity predicted from CPFE simulations. Grains in which prismatic activity was predicted from CPFE simulations include all grains except grains N and Q. In the CPFE simulations, grain A, O, M and R show both prismatic and

pyramidal $<a>$ activity, some twin activity is seen in grain B. Grains P, Q and N show pyramidal $<a>$ activity in the CPFE model and is confirmed with the DIC slip traces. Note that pyramidal $<a>$ has often not been used in Mg alloy CPFE simulations [42,43], but from the current simulations and experiments, these slip systems do indeed play a role in deformation of WE43-T5 and should be included. Some grains have multiple slip systems active as seen from the CPFE simulations. For example, CPFE simulations indicate that grain N has both basal (as seen in Fig. 15) and pyramidal $<a>$ slip active and these simulation results were confirmed with the slip trace analysis.

Some of the grains show two traces in the data, but since traces are not available in CPFE simulations we threshold them to identify if two traces will be seen. Two traces are included in computing the histogram plot in Fig. 7 (b) if the resolved strain ratio for second most active to most active system is greater than 70%. This data was obtained from a statistically representative microstructure and the histogram was normalized such that 130 total traces are plotted (similar to the DIC data).in Fig. 7(b). We find that non-basal slip in grains with higher non-basal Schmid factor are over predicted in the CPFE simulation. Twinning is relatively lower compared to the DIC data in Fig. 7(a).

There are some discrepancies between the results of the CPFE simulation and experimental slip traces observed in a few grains. For example, Grain A and P shows experimental slip traces that correspond to extension twinning. However, grain P shows no twinning in CPFE simulations and, rather, prismatic slip predicted. Likewise, the simulation showed that in grain A pyramidal $<a>$ slip activity was expected however extension twinning was observed by DIC slip trace analysis. It should be noted that the angular difference between the trace for extension twinning in grains A observed by DIC and the pyramidal $<a>$ system predicted by CPFE is only 5.9 degrees apart. This small difference is nearly indistinguishable in experimental measurements. CPFE can thus be used to correctly classify the traces observed in the DIC data. If a grain deforms via basal slip, strain accommodation in the neighboring grains may necessitate the activation of non-basal systems. The fact that multiple slip systems can be active within a grain (e.g. grain A) and slip activity of a system can be localized within a grain to one side (Fig. 6(c) of DIC, or prismatic slip in grain B in Fig. 16) demonstrated that significant deviations can occur in grain to grain strains.

The predominant slip systems in CPFE is calculated by comparing the averaged strain contribution of each slip system to each grain. The first and second predominant slip trace are computed
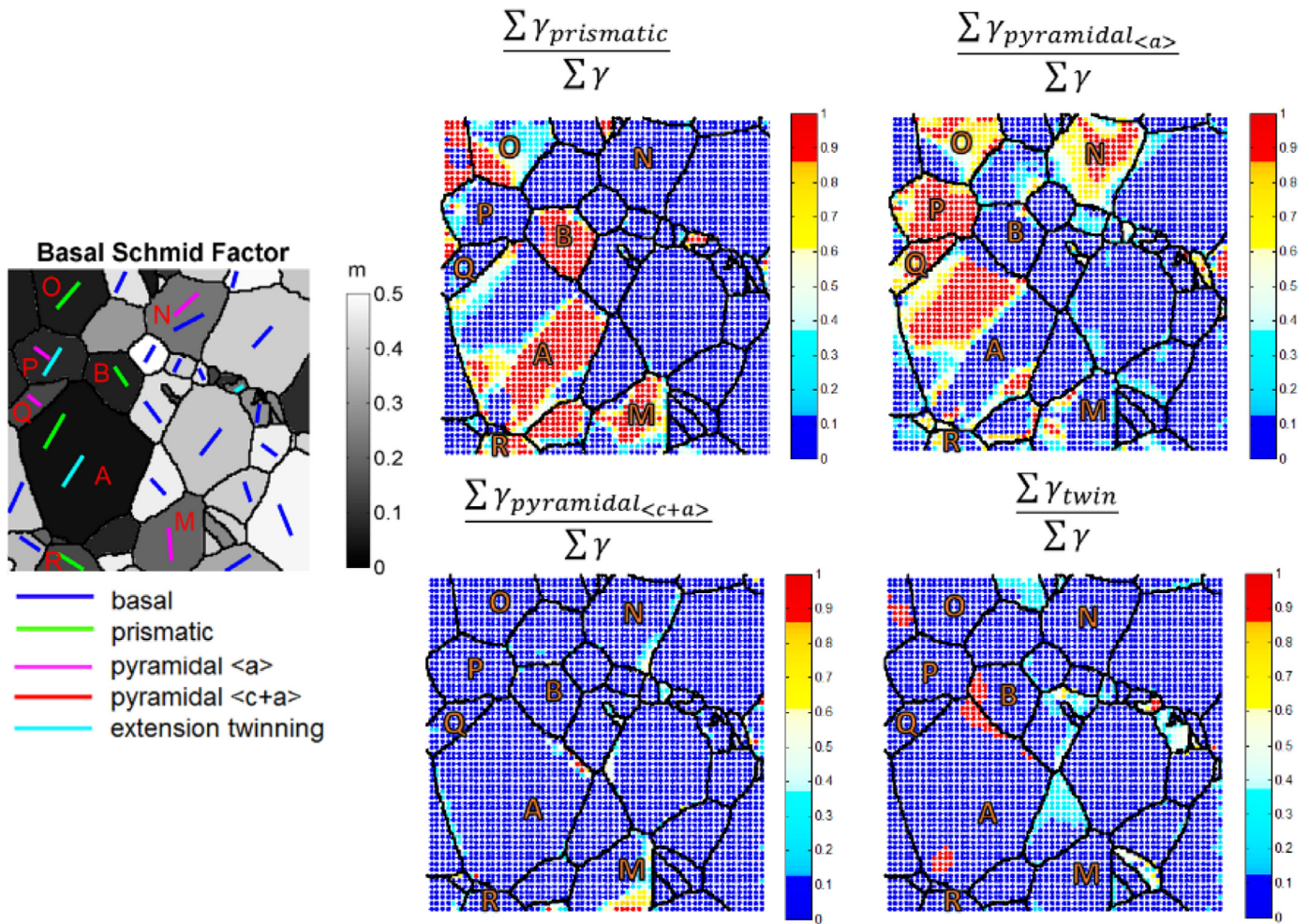
Fig. 16. Slip traces from the SEM-DIC data (left) are compared with the slip activity for grains that deform through a non-basal mechanism predicted using the CPFE simulation.
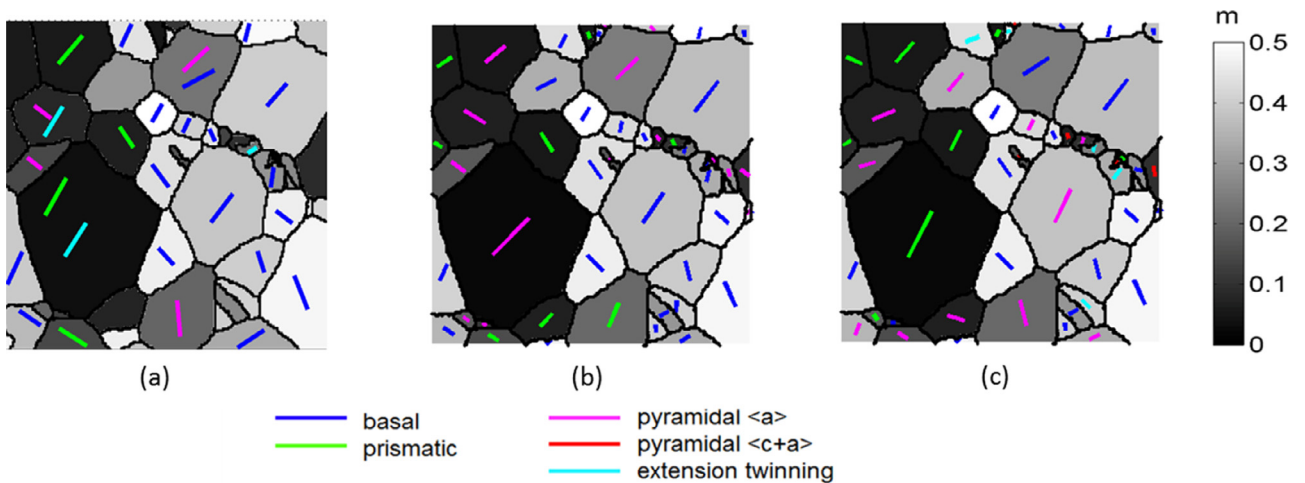

Fig. 17. Slip traces from the SEM-DIC image (a) are compared with the first predominant slip trace (b) and second predominant slip trace (c) predicted by the CPFE-DIC simulations.

by plotting the slip normal direction of the corresponding slip systems as shown in Fig. 17(b) and (c). From these plots, we can define a metric for matching the slip traces between DIC images and CPFE simulations called the slip-trace matching error. It is defined as the ratio of mismatched slip traces between DIC images (Fig. 17 (a) and CPFE simulations (Fig. 17 (b) and (c)) to the total num-

ber of traces in the DIC image. In the current study, 5 slip traces were mismatched out of 28, therefore the slip-trace matching error is 0.179 or 17.9%. Jonas et al. found that strain accommodation in neighboring grains played a key role in twinning variant selection and justified similar deviations from correlations with the nominal Schmid behavior during compressive loading of AM30 and AZ31
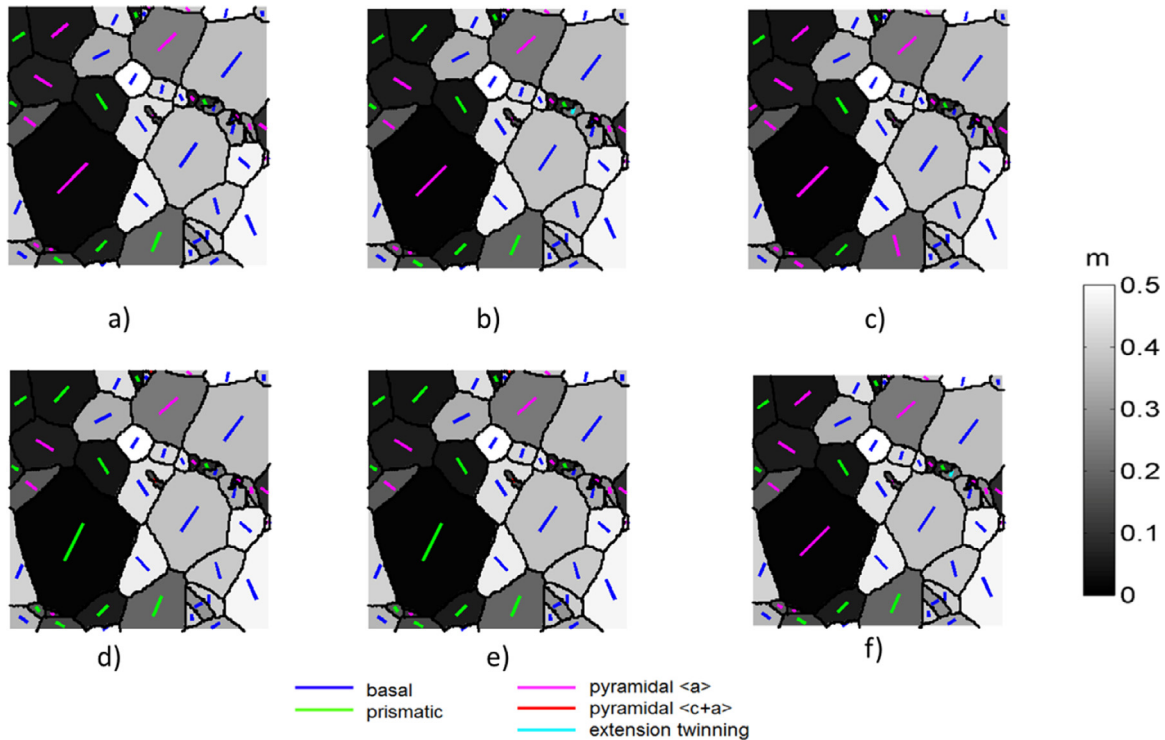
Fig. 18. Comparison of predominant slip trace from CPFE simulations for sensitivity analysis in CRSS (a) Baseline (b) Case 1 (c) Case 2 (d) Case 3 (e) Case 4 (f) Case 5.

Table 4
Sensitivity study of slip activity with respect to CRSS values.

	Baseline	Case 1	Case 2	Case 3	Case 4	Case 5
Basal $<a>$	76.0	79.8	76.0	76.0	76.0	76.0
Prism $<a>$	163.2	163.2	171.4	163.2	163.2	163.2
Pyram $<a>$	160.3	160.3	160.3	168.3	160.3	160.3
Pyram$<c+a>$	187.4	187.4	187.4	187.4	196.8	187.4
Twin$<c+a>$	116.4	116.4	116.4	116.4	116.4	122.2
Slip-trace matching error (%)	17.9	10.7	17.9	14.2	14.2	14.2

alloys [45]. It may also be a reason that the macroscopic loading may dictate the activation of basal slip, and the deforming basal slip systems subsequently dictate the activation of non-basal and other basal systems.

A sensitivity study was conducted by varying the CRSS values of the slip systems by 5 %. The CRSS values of individual cases which were studied are tabulated in Table 4. The predominant traces are compared with the baseline CRSS values in Fig. 18 (a)-(f). The CRSS values in each study and the corresponding slip-trace matching error are tabulated in Table 4. Case 1, with an increase in basal CRSS shows the closest match with the minimum slip-trace matching error followed by Case 3, which has pyramidal$<a>$ CRSS greater than prismatic CRSS. All the cases show differences from the baseline in terms of slip-trace matching error. This shows that the study is sensitive to all the slip systems and specifically pyramidal slip systems in this particular alloy. This also suggests that 79.8MPa is a slightly superior value for the basal slip critical resolved shear stress for this alloy and heat treatment condition.

4.3. CPFE simulations with 3-D microstructure

To study of the effect of variability associated with 3D microstructure, 3D microstructures were computationally generated with the same surface grain structure but differences in the 3D grain distribution [46]. Using a Voronoi approach [46], two variants

were generated with voronoi centers placed to retrieve an average grain size of 12 microns while maintaining the surface image. Variant 1 comprises of 340 grains and variant 2 comprises of 367 grains as seen in Fig. 19(b) and (c). Orientations were assigned such that the texture for all three cases are equivalent. Since Voronoi method leads to convex grains, we have also convexified the real microstructure so the results can be compared to the 3D reconstructions [46]. The displacement boundary conditions used for columnar grains are applied to the resultant 3D microstructure. Since the 3D boundary conditions are unknown, we have primarily extended these displacements along the z-axis. Simulations for columnar, variant 1 and variant 2 microstructures were performed with a mesh of $100 \times 100 \times 100$ elements using PRISMS-Plasticity code. The results of the simulations are discussed below

Individual grains A-N are marked in Fig. 21(a), (b) and (c) to study the variation in strain between columnar microstructures and the 3D variants of the microstructures as seen in Fig. 20(b), (c) and (d). We see that the surface strain maps are similar across the three cases in Fig. 20(b), (c) and (d). Since the surface is traction free, a choice of generalized plane-stress (2D) on a columnar grain structure appears reasonable. To understand this result better, we have also compared the relative activity of the individual slip systems in Fig. 21(a), (b) and (c). While the grains with orientation favorable for basal slip show similar activity in 2D vs 3D cases, there are differences in grains with non-basal activity as shown by a couple of examples:

- Grain A shows predominantly prismatic activity in columnar microstructure and variant 1, while it shows a region of pyramidal $<a>$ activity in variant 2 as seen in Fig. 21(a), (b) and (c)
- Grain B shows pyramidal $<c + a>$ activity for columnar microstructure and variant 1, whereas it shows predominantly prismatic slip activity in variant 2 as seen in Fig. 21(a), (b) and (c)
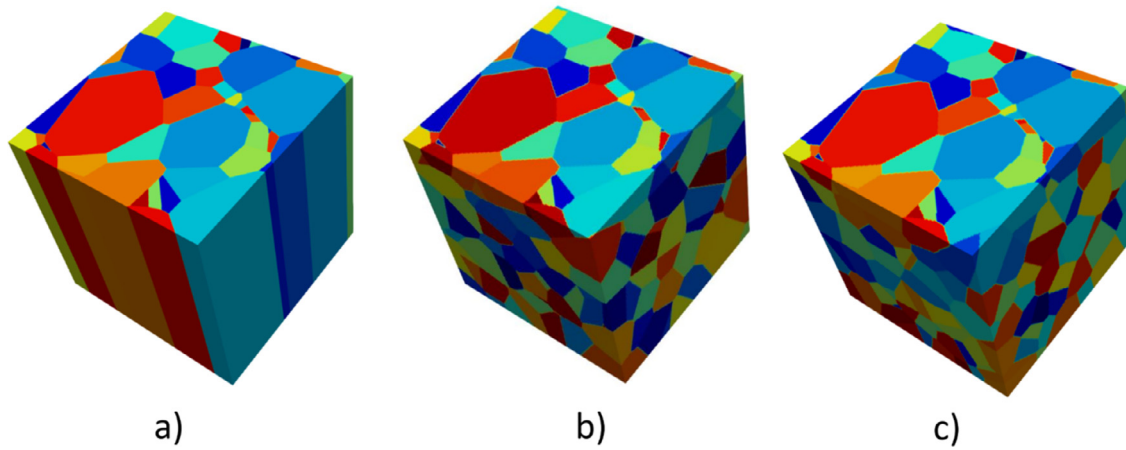
Fig. 19. Microstructures considered in this study (a) Convexified columnar microstructure (b) variant 1 of 3d microstructure (c) variant 2 of 3d microstructure.
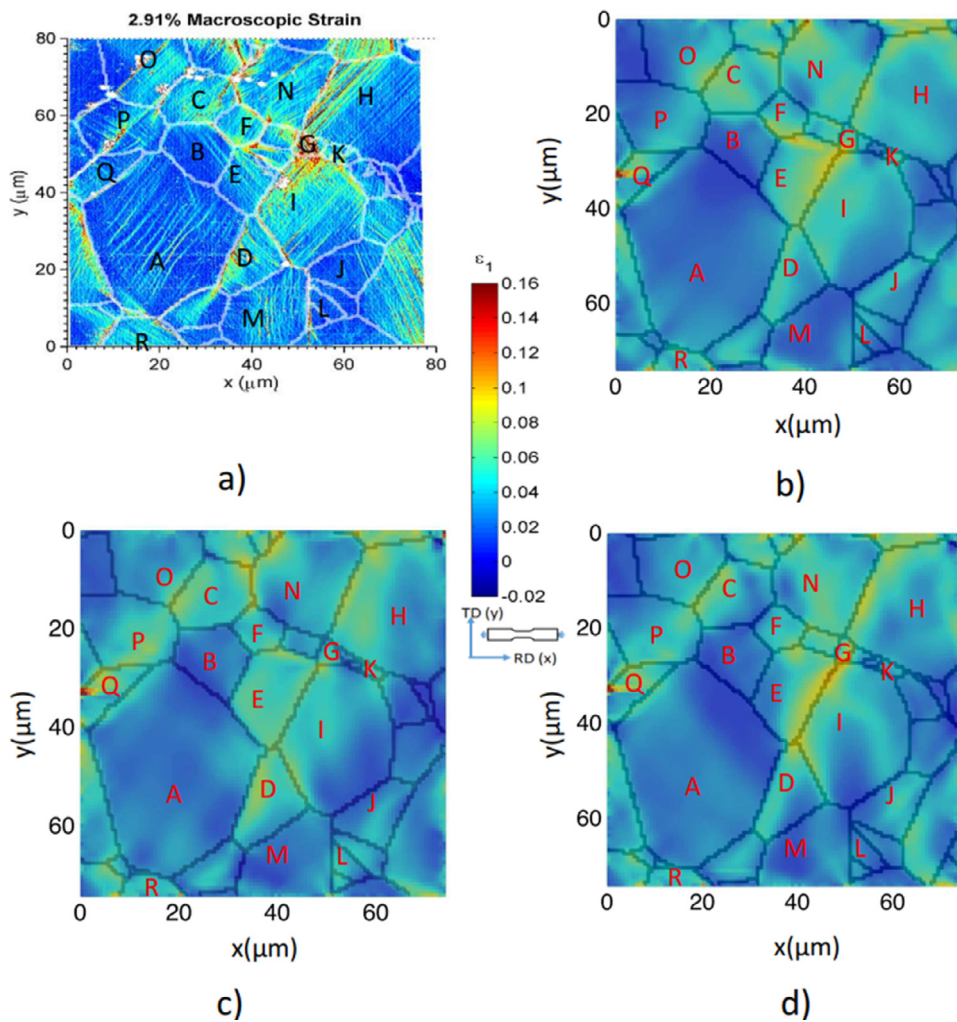

Fig. 20. Comparison of CPFE principal strain 1 from (a) Real microstructure (b) Convexified columnar microstructure (b) 3d variant 1 (c) 3d variant 2.

These changes (as expected) are a result of the 3D microstructure. Variations in non-basal activity occur due to 3D grain structure when strong basal slip activation occurring in underlying grains triggers other non-basal systems in surface grains with low basal Schmid factor. From a study of the slip activity at different depths of the material for the 3D variant 2 as shown in Fig. 22, we observe that in case of both grain A and B where we see prismatic or pyramidal-a activity that there are grains underneath the surface which show strong basal slip activity. The variation in the basal activity with cross sections at various depths of
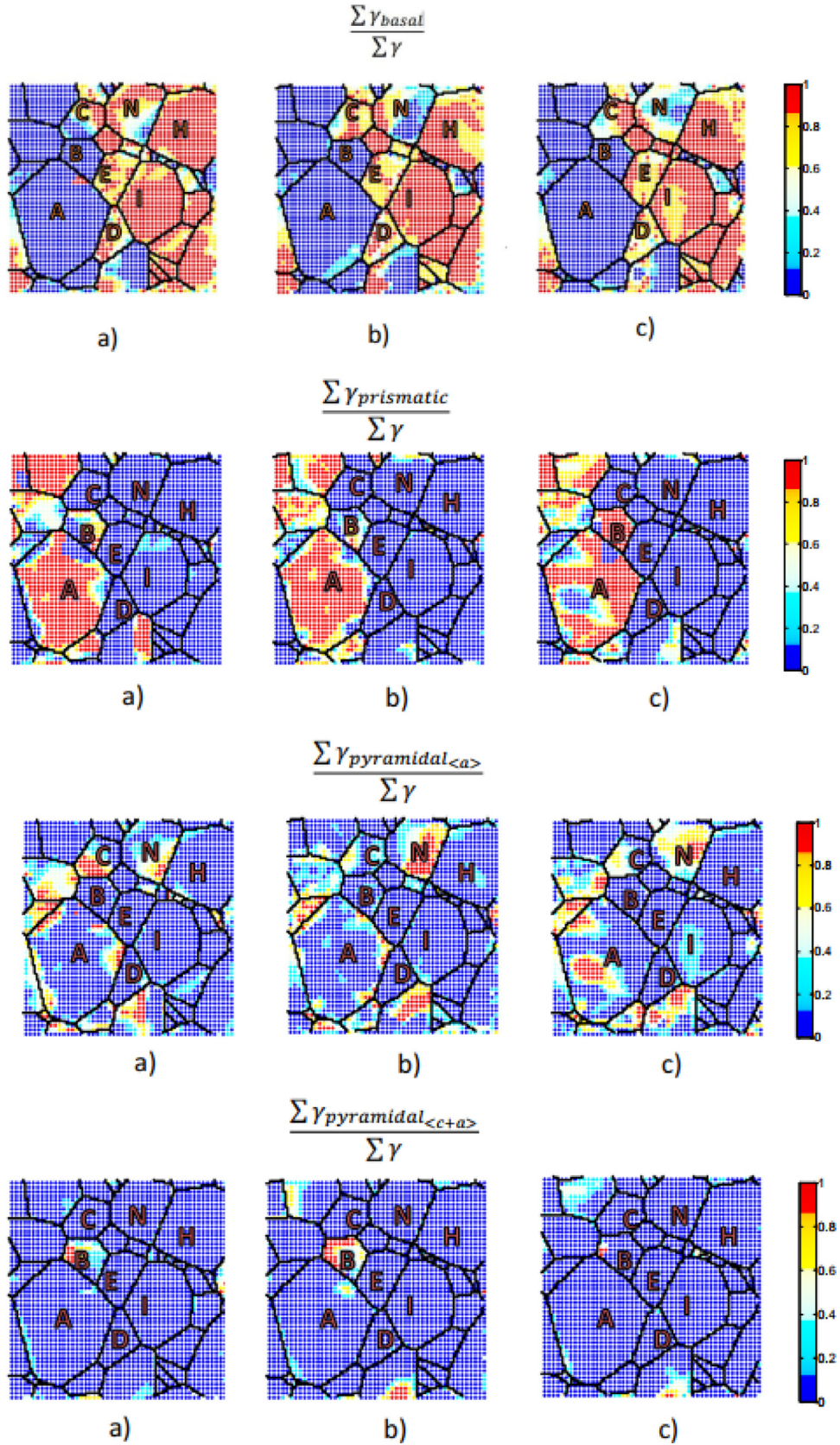
$$\frac{\sum \gamma_{basal}}{\sum \gamma}$$

a)   b)   c)

$$\frac{\sum \gamma_{prismatic}}{\sum \gamma}$$

a)   b)   c)

$$\frac{\sum \gamma_{pyramidal_{<a>}}}{\sum \gamma}$$

a)   b)   c)

$$\frac{\sum \gamma_{pyramidal_{<c+a>}}}{\sum \gamma}$$

a)   b)   c)

Fig. 21. Normalized resolved shear strain for different slip systems (a) columnar (b) 3d variant 1 (c) 3d variant 2.

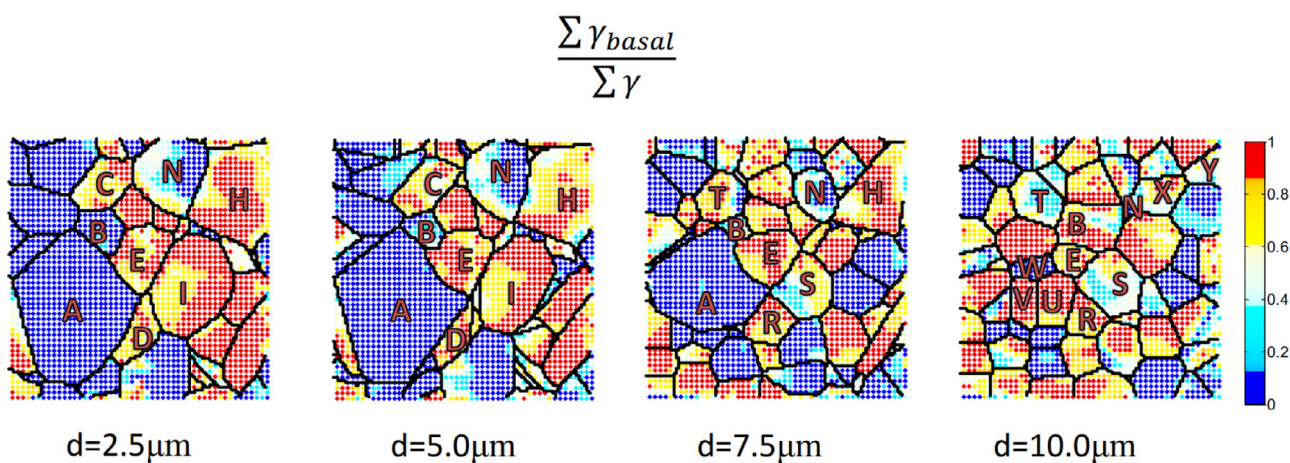$$\frac{\sum \gamma_{basal}}{\sum \gamma}$$

Fig. 22. Normalized resolved shear strain for basal slip of 3d variant 2 along the depth direction.

microstructure variant2 is in Fig. 22. We observe that grains V and U have a strong basal slip underneath A. The island of pyramidal$<a>$ slip observed on the surface is triggered by these grains.

5. Conclusions

Full-field plastic strains were characterized for the magnesium alloy WE43 in a hot rolled plate in the T5 heat treatment condition. Due to the high resolution possible with *in-situ* SEM imaging combined with digital image correlation, the quantified strain from individual slip traces was measured for the first time in magnesium. This data was used in a unique way to validate the results of the PRISMS-Plasticity CPFE simulations. The quantification of strain allowed for the following insights on the deformation mechanisms that occur during plastic deformation: In both tension and compression, strain localization occurred at the onset of global yielding and the strain heterogeneity remained fairly constant with increasing macroscopic strain. The strain of a given slip system can vary significantly between different grains as well as within the same grain. In tension, basal and non-basal slip activation was correlated with high nominal Schmid factor for the appropriate slip system. In compression, basal slip and extension twinning dominated the deformation and were both correlated with high nominal Schmid factors.

The DIC results were compared with crystal plasticity finite element (CPFE) simulations and the strain distribution is captured reasonably well by the model. The CPFE model is able to identify local Schmid factor variations due to the effect of neighbor grains in the form of relative slip activity, and thus computationally differentiate the slip traces observed in the DIC data into various slip and twin systems. The first and second predominant slip/twin systems from CPFE method and the DIC slip trace analysis were directly compared. From this analysis, we are able to differentiate between the three types of basal slip systems that correspond to the same basal slip trace and identify the activated slip/twin systems in cases where the traces are near indistinguishable. Deviations of CPFE model from DIC data in the tensile loading case primarily occur in regions with small grains and in regions where DIC data show significant grain boundary localizations of strains – and we identify these as areas for improvement of CPFE models. The plastic deformation band developing at the surface shows dependency on the 3D morphology of the grains beneath the surface. The results presented in this work show the implications of performing a full 3D finite element analysis of the problem as compared to the 2D approach. The combined use of DIC, EBSD and CPFE provide an effective means to improve our understanding of the CRSS of all active slip systems.

Declaration of Competing Interest

The authors declare that they have no known competing financial interests or personal relationships that could have appeared to influence the work reported in this paper.

Supplementary materials

Supplementary material associated with this article can be found, in the online version, at doi:10.1016/j.actamat.2019.12.012.

References

[1] "PRISMS-Plasticity open source crystal plasticity code https://github.com/prisms-center/plasticity, retrieved Jan 13, 2017".

[2] M. Yaghoobi, S. Ganesan, S. Sundar, A. Lakshmanan, S. Rudraraju, J.E. Allison, V. Sundararaghavan, PRISMS-Plasticity: An open-source crystal plasticity finite element software, Comput. Mater. Sci. 169 (2019) 109078.

[3] L. Aaegesen, et al., PRISMS- an integrated, open source framework for accelerating predictive structural materials science, J. Mech. 70 (10) (2018) 2298–2314.

[4] A. Jain, S.R. Agnew, Modeling the temperature dependent effect of twinning on the behavior of magnesium alloy AZ31B sheet, Mater. Sci. Eng. A 462 (Jul. 2007) 29–36.

[5] M.R. Barnett, Twinning and the ductility of magnesium alloys, Mater. Sci. Eng. A 464 (Aug. 2007) 1–7.

[6] M.R. Barnett, Twinning and the ductility of magnesium alloys, Mater. Sci. Eng. A 464 (Aug. 2007) 8–16.

[7] C.M. Cepeda-Jiménez, J.M. Molina-Aldareguia, M.T. Pérez-Prado, Effect of grain size on slip activity in pure magnesium polycrystals, Acta Mater. 84 (Feb. 2015) 443–456.

[8] C.J. Boehlert, Z. Chen, I. Gutiérrez-Urrutia, J. Llorca, M.T. Pérez-Prado, In situ analysis of the tensile and tensile-creep deformation mechanisms in rolled AZ31, Acta Mater. 60 (4) (Feb. 2012) 1889–1904.

[9] B. Raeisinia, S.R. Agnew, A. Akhtar, Incorporation of solid solution alloying effects into polycrystal modeling of Mg alloys, Metall. Mater. Trans. A 42 (5) (Nov. 2010) 1418–1430.

[10] S.R. Agnew, R.P. Mulay, F.J. Polesak, C.A. Calhoun, J.J. Bhattacharyya, B. Clausen, In situ neutron diffraction and polycrystal plasticity modeling of a Mg–Y–Nd–Zr alloy: Effects of precipitation on individual deformation mechanisms, Acta Mater. 61 (10) (Jun. 2013) 3769–3780.

[11] H. Li, D.E. Mason, T.R. Bieler, C.J. Boehlert, M.A. Crimp, Methodology for estimating the critical resolved shear stress ratios of α-phase Ti using EBSD-based trace analysis, Acta Mater. 61 (20) (Dec. 2013) 7555–7567.

[12] S.R. Agnew, Ö. Duygulu, Plastic anisotropy and the role of non-basal slip in magnesium alloy AZ31B, Int. J. Plast. 21 (6) (Jun. 2005) 1161–1193.

[13] G. Martin, C.W. Sinclair, R.A. Lebensohn, Microscale plastic strain heterogeneity in slip dominated deformation of magnesium alloy containing rare earth, Mater. Sci. Eng. A 603 (May 2014) 37–51.

[14] V. Sundararaghavan, N. Zabaras, A multi-length scale continuum sensitivity analysis for the control of texture-dependent properties in deformation processing, Int. J. Plast. 24 (9) (2008) 1581–1605.

[15] S. Sun, V. Sundararaghavan, A Peridynamic Implementation of Crystal Plasticity, Int. J. Solids Struct. 51 (19–20) (2014) 3350–3360.

[16] V. Sundararaghavan, A. Kumar, S. Sun, Crystal plasticity simulations using nearest neighbor orientation correlation function, Acta Mater. 93 (2015) 12–23.

[17] S. Sun, V. Sundararaghavan, A probabilistic crystal plasticity model for modeling grain shape effects based on slip geometry, Acta Mater 60 (13–14) (2012) 5233–5244.

[18] L. Anand, M. Kothari, A computational procedure for rate-independent crystal plasticity, J. Mech. Phys. Solids 44 (4) (1996) 525–558.

[19] M.A. Sutton, J.J. Orteu, H.W. Schreier, in: Image Correlation for Shape, Motion, and Deformation Measurements, Springer Science+Business Media, LLC, 2009, p. 321.

[20] M.R. Barnett, S. Jacob, B.F. Gerard, J.G. Mullins, Necking and failure at low strains in a coarse-grained wrought Mg alloy, Scr. Mater. 59 (10) (Nov. 2008) 1035–1038.

[21] N. Stanford, K. Sotoudeh, P.S. Bate, Deformation mechanisms and plastic anisotropy in magnesium alloy AZ31, Acta Mater 59 (12) (Jul. 2011) 4866–4874.

[22] R.A. Lebensohn, R. Brenner, O. Castelnau, A.D. Rollett, Orientation image-based micromechanical modelling of subgrain texture evolution in polycrystalline copper, Acta Mater. 56 (2008) 3914–3926.

[23] H. Abdolvand, M. Majkut, J. Oddershede, S. Schmidt, U. Lienert, B.D. Diak, P.J. Withers, M.R. Daymond, On the deformation twinning of Mg AZ31B: a 3D synchrotron X-ray diffraction experiment and crystal plasticity finite element model, Intl. J. Plasticity 70 (2015) 77–97.

[24] G. Martin, C.W. Sinclair, J.-H. Schmitt, Plastic strain heterogeneities in an Mg–1Zn–0.5Nd alloy, Scr. Mater. 68 (May 2013) 695–698.

[25] N. Stanford, M.R. Barnett, The origin of 'rare earth' texture development in extruded Mg-based alloys and its effect on tensile ductility, Mater. Sci. Eng. A 496 (Nov. 2008) 399–408.

[26] N. Stanford, M. Barnett, Effect of composition on the texture and deformation behaviour of wrought Mg alloys, Scr. Mater. 58 (3) (Feb. 2008) 179–182.

[27] J.F. Adams, J.E. Allison, J.W. Jones, The effects of heat treatment on very high cycle fatigue behavior in hot-rolled WE43 magnesium, Int. J. Fatigue 93 (2016) 372–386.

[28] A. Githens, S. Daly, Patterning corrosion-susceptible metallic alloys for digital image correlation in a scanning electron microscope, Strain 53 (1) (2016).

[29] J.F. Nie, B.C. Muddle, Characterisation of Strengthening Precipitate Phases in a Mg–Y–Nd Alloy, Acta Mater. 48 (May 2000) 1691–1703.

[30] C. Antion, P. Donnadieu, F. Perrard, a. Deschamps, C. Tassin, a. Pisch, Hardening precipitation in a Mg–4Y–3RE alloy, Acta Mater. 51 (18) (Oct. 2003) 5335–5348.

[31] G. Barucca, R. Ferragut, F. Fiori, D. Lussana, P. Mengucci, F. Moia, G. Riontino, Formation and evolution of the hardening precipitates in a Mg–Y–Nd alloy, Acta Mater. 59 (10) (Jun. 2011) 4151–4158.

[32] E. Sitzmann, E.A. Marquis, Chemistry and morphology of β' precipitates in an aged Mg-Nd-Y-Zr alloy, Philos. Mag. Lett. 95 (1) (Feb. 2015) 7–13.

[33] J. Nie, Precipitation and hardening in magnesium alloys, Metall. Mater. Trans. A 43A (Jul. 2012) 3891–3939.

[34] A.R. Natarajan, E.L.S. Solomon, B. Puchala, E.A. Marquis, A. Van der Ven, On the early stages of precipitation in dilute Mg-Nd alloys, Acta Mater. 108 (2016) 367–379.

[35] A.R. Natarajan, A. Van der Ven, A unified description of ordering in HCP Mg-RE alloys, Acta Mater. 124 (2017) 620–632.

[36] E.L.S. Solomon, V. Araullo-Peters, J.E. Allison, E.A. Marquis, Early precipitate morphologies in Mg-Nd-(Zr) alloys, Scr. Mater. 128 (2017) 14–17.

[37] E.L.S. Solomon, E.A. Marquis, Deformation behavior of β' and β'' precipitates in Mg-RE alloys, Mater. Lett. 216 (1) (2018) 67–69.

[38] A.D. Kammers, S. Daly, Digital image correlation under scanning electron microscopy: methodology and validation, Exp. Mech. 53 (Jul. 2013) 1743–1761.

[39] C.N. Tomé, R.A. Lebensohn, U.F. Kocks, A model for texture development dominated by deformation twinning: Application to zirconium alloys, Acta Metall. Mater. 39 (11) (1991) 2667–2680.

[40] R.F.S. Hearmon, The elastic constants of crystals and other anisotropic materials, Landolt-Börnstein Tables 3 (18) (1984) 559.

[41] R. Quey, P.R. Dawson, F. Barbe, Large-scale 3D random polycrystals for the finite element method: Generation, meshing and remeshing, Comput. Methods Appl. Mech. Eng. 200 (17–20) (2011) 1729–1745.

[42] N. Stanford, R. Cottam, B. Davis, J. Robson, Evaluating the effect of yttrium as a solute strengthener in magnesium using in situ neutron diffraction, Acta Mater. 78 (2014) 1–13.

[43] J.J. Bhattacharyya, F. Wang, P.D. Wu, W.R. Whittington, H. El Kadiri, S.R. Agnew, Demonstration of alloying, thermal activation, and latent hardening effects on quasi-static and dynamic polycrystal plasticity of Mg alloy, WE43-T5, plate, Int. J. Plast. 81 (2016) 123–151.

[44] S. Forest, Modeling slip, kink and shear banding in classical and generalized single crystal plasticity, Acta Mater. 46 (9) (1998) 3265–3281.

[45] J.J. Jonas, S. Mu, T. Al-Samman, G. Gottstein, L. Jiang, È. Martin, The role of strain accommodation during the variant selection of primary twins in magnesium, Acta Mater. 59 (5) (2011) 2046–2056 Mar..

[46] S. Ganesan, Microstructural Response of Magnesium Alloys: 3D Crystal Plasticity and Experimental Validation Ph.D. Thesis, University of Michigan, Ann Arbor, 2017.

[47] B. Puchala, G. Tarcea, E.A. Marquis, M. Hedstrom, H.V. Jagadish, J.E. Allison, The materials commons: a collaboration platform and information repository for the global materials community, JOM 68 (8) (2016) 2035–2044.